UNIVERSIDADE DE SÃO PAULO
ESCOLA DE ENGENHARIA DE SÃO CARLOS

Blanca Prior Palomero

Computational Fluid Dynamics Analysis of a Waverider Configuration

São Carlos

2025

Blanca Prior Palomero

Computational Fluid Dynamics Analysis of a Waverider Configuration

Monografia apresentada ao Curso de Engenharia Aeronáutica, da Escola de Engenharia de São Carlos da Universidade de São Paulo, como parte dos requisitos para obtenção do título de Engenheiro Aeronáutico.

Advisor: Prof. Dr. Hernán Dario Cerón-Muñoz

São Carlos

2025

Cataloging-in-publication data prepared by the Prof. Sérgio Rodrigues Fontes Library and the Communication and Marketing Office at EESC-USP, with information provided by the author.

P958c

Prior Palomero, Blanca

Computational Fluid Dynamics Analysis of a Waverider Configuration / Blanca Prior Palomero ; advisor Hernan Dario Ceron-Muñoz. -- São Carlos, .

p.

Undergraduate Thesis in Aeronautical Engineering -- São Carlos School of Engineering of University of São Paulo, .

1. Computational Fluid Dynamics. 2. Hypersonic vehicle. 3. Aerodinamics,. I. Hernan Dario, Ceron-Muñoz, advisor. II. Título.

Responsible for the cataloging structure of the publication according to AACR2: EESC Librarians

FOLHA DE APROVAÇÃO
Approval sheet

Candidato / *Student*: Blanca Prior Palomero
Título do TCC / *Title* **:** Computational Fluid Dynamics Analysis of a Waverider Configuration
Data de defesa / *Date*: 25/09/2025

Comissão Julgadora / *Examining committee*	**Resultado** / *result*
Professor Associado Hernan Dario Cerón Muñoz	APROVADO
Instituição / Affiliation: EESC - SAA	
Professor Doutor João Paulo Eguea	APROVADO
Instituição / Affiliation: EESC - SAA	
Doutor Pedro David Bravo Mosquera	APROVADO
Instituição / Affiliation: EESC - SAA	

Presidente da Banca / Chair of the Examining Committee:

Professor Doutor Hernán Dario Cerón- Muñoz
(assinatura / *signature*)

This work is dedicated to Isabel Moro,
because there is no rush, so what's one more year?

ACKNOWLEDGEMENTS

First of all, I am eternally grateful to MaritaConforto, Josem8, AeroSalvada, An27ita and Rosarub, without whom I would have never reached this moment or managed to complete my degree.

To my friends and sisters here in Brasil, Vai da Nada truly feels like home. Thank you for taking a chance on me and making this experience unforgettable.

I profoundly express my gratitude to the professor Hernán Cerón-Muñoz and Rolando Guzman-Bohórquez for its patience, guidance, and support.

Lastly, to my family and friends, from classmates to flatmates, who were just as much a part of this phase, that is now coming to a close.

"What we observe is not nature itself, but nature exposed to our method of questioning."
Werner Heisenberg, Physics and Philosophy: The Revolution in Modern Science

ABSTRACT

PRIOR PALOMERO, B. **Computational Fluid Dynamics Analysis of a Waverider Configuration**. 2025. 87 p. Monograph (Conclusion Course Paper) - Escola de Engenharia de São Carlos, Universidade de São Paulo, São Carlos, 2025.

This study simulates the aerodynamic behavior of a wedge configuration, which serves as a fundamental model for a waverider, under hypersonic flow conditions using the SU2 software. Rather than focusing on optimized geometries, this work establishes a baseline for hypersonic analysis, aiming to validate the computational framework, test numerical schemes, mesh strategies, and boundary conditions, and analyze aerodynamic coefficients under varying Mach numbers and angles of attack. The results demonstrate successful convergence with minimal residuals, confirming the reliability of the numerical simulations.

The findings highlight the sensitivity of shock structure and aerodynamic loading to Mach number and angle of attack. Specifically, variations in Mach number and angle of attack significantly impact pressure distributions and the shock structure, with angle of attack redistributing the shock location and intensity, affecting both the upper and lower surface flow characteristics. The study emphasizes the critical importance of geometric optimization in hypersonic vehicle design, with even minor changes in angle of attack resulting in substantial shifts in aerodynamic behavior.

In terms of aerodynamic coefficients, the analysis reveals a complex interplay between shock wave effects, pressure coefficient distributions, and the lift-to-drag ratio. As the angle of attack increases, the shock structure intensifies, particularly affecting the compression on the lower surface and expansion on the upper surface. The lift-to-drag ratio improves moderately with increased lift, though the concurrent rise in drag limits this enhancement.

Comparisons with analytical solutions show good agreement, but discrepancies in the shock and expansion zones suggest that a refined mesh near the leading edge would improve the resolution of shock-flow interactions. Additionally, the study highlights the need for re-evaluating assumptions such as the neglect of viscosity, which is essential for enhancing accuracy under extreme conditions.

Keywords: Aerodynamics. Hypersonic Flow. Hypersonic Vehicle. Waverider.

RESUMO

PRIOR PALOMERO, B. **Análise de Dinâmica dos Fluidos Computacional de uma Configuração Waverider**. 2025. 87 p. Monografia (Trabalho de Conclusão de Curso) - Escola de Engenharia de São Carlos, Universidade de São Paulo, São Carlos, 2025.

Este estudo simula o comportamento aerodinâmico de uma configuração de cunha, que serve como modelo fundamental para um waverider, sob condições de fluxo hipersônico utilizando o software SU2. Em vez de focar em geometrias otimizadas, este trabalho estabelece uma linha de base para a análise hipersônica, com o objetivo de validar a estrutura computacional, testar esquemas numéricos, estratégias de malha e condições de contorno, além de analisar os coeficientes aerodinâmicos sob diferentes números de Mach e ângulos de ataque. Os resultados demonstram a convergência bem-sucedida com resíduos mínimos, confirmando a confiabilidade das simulações numéricas.

Os resultados destacam a sensibilidade da estrutura do choque e da carga aerodinâmica ao número de Mach e ao ângulo de ataque. Especificamente, as variações no número de Mach e no ângulo de ataque impactam significativamente as distribuições de pressão e a estrutura do choque, com o ângulo de ataque redistribuindo a localização e a intensidade do choque, afetando tanto as características de fluxo na superfície superior quanto na superfície inferior. O estudo enfatiza a importância crítica da otimização geométrica no projeto de veículos hipersônicos, com até pequenas alterações no ângulo de ataque resultando em mudanças substanciais no comportamento aerodinâmico.

Em termos de coeficientes aerodinâmicos, a análise revela uma interação complexa entre os efeitos da onda de choque, as distribuições de coeficiente de pressão e a relação de sustentação-arrasto. À medida que o ângulo de ataque aumenta, a estrutura do choque se intensifica, afetando particularmente a compressão na superfície inferior e a expansão na superfície superior. A relação de sustentação-arrasto melhora moderadamente com o aumento da sustentação, embora o aumento concomitante do arrasto limite essa melhoria.

Comparações com soluções analíticas mostram boa concordância, mas as discrepâncias nas zonas de choque e expansão sugerem que uma malha refinada próxima à borda de ataque melhoraria a resolução das interações de choque e fluxo. Além disso, o estudo destaca a necessidade de reavaliar suposições, como a negligência da viscosidade, essencial para melhorar a precisão em condições extremas.

Palavras-chave: Aerodinâmica. Escoamento Hipersônico. Veículo Hipersônico. Waverider.

LIST OF FIGURES

LIST OF TABLES

LIST OF ABBREVIATIONS AND ACRONYMS

CFD	Computational Fluid Dynamics
CFL	Courant-Friedrichs-Lewy Number
DARPA	Defense Advanced Research Projects Agency
EFSEFD	Endothermically Fueled Scramjet Engine Flight Demonstrator
FGMRES	Flexible Generalized Minimal Residual
HCV	Hypersonic Cruise Vehicles
HFV	Hypersonic Flight Vehicles
HGV	Hypersonic Boost-Glide Vehicles
HTT	Hypersonic Transport Technology
HTV	Hypersonic Technology Vehicle
HyCAUSE	Hypersonic Collaborative Australian/United States Experiment
ISA	International Standard Atmosphere
JPL	Jet Propulsion Laboratory
LU_SGS	Lower-Upper Symmetric Gauss-Seidel
NASA	National Aeronautics and Space Administration
PDE	Partial Differential Equations
RAE	The Royal Aircraft Establishment
SED-WR	Scramjet Engine Demonstrator-WaveRider
SLS	Space Launch System
SLV	Small Launch Vehicle
SOAREX	Sub-Orbital Aerodynamic Re-entry EXperiments
USAF	United States Air Force
USP	Universidade de São Paulo
USPSC	Campus USP de São Carlos
WASP	Waverider Aerodynamic Study Program

LIST OF SYMBOLS

C_L	Lift Coefficient
C_D	Drag Coefficient
L	Wedge Reference Length
b	Wedge Span
z	Wedge Height
V	Wedge Internal Volume
S_{wetted}	Wetted Area
h	Altitude
M_∞	Freestream Mach Number
P_∞	Freestream Static Pressure
T_∞	Freestream Temperature
AoA	Angle of Attack
ρ	Density
p	Pressure
R	Specific gas constant
u	Velocity in the x-axis
v	Velocity in the y-axis
w	Velocity in the z-axis

CONTENTS

1 INTRODUCTION AND JUSTIFICATION

Hypersonic vehicles have emerged as a key area of study for aerospace engineering due to their potential for long-range precision strikes and a variety of applications such as emergency response, business travel, and military operations. Hypersonic Flight Vehicles (HFV), which include both Hypersonic Cruise Vehicles (HCV) and Hypersonic Boost-Glide Vehicles (HGV), are defined by their ability to travel at speeds exceeding **Mach 5**, offering a cost-efficient means to access space and allowing rapid global reach. These vehicles' main advantage lies in their low resistance and energy consumption at high speeds, which makes them perfect for time-sensitive applications. Developed nations are making large investments in this technology, despite the considerable challenges related to their development, design complexity and material stress under extreme conditions.

Figure 1 – Classification of hypersonic vehicles.

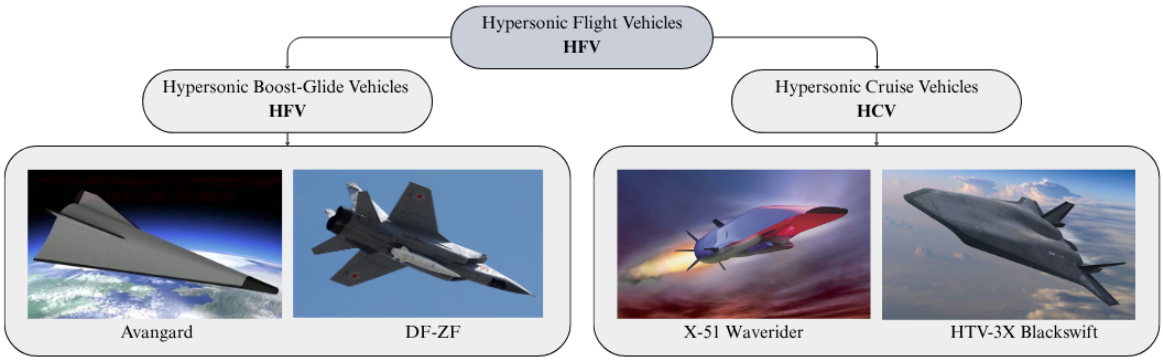

Source: Author.

The success of hypersonic vehicle development depends not only on the vehicles themselves but also on a more comprehensive systems approach that takes **safety, security, maintainability, operational flexibility, reliability, and sustainability** into account. Aircraft manufacturers are focused on creating more efficient and environmentally friendly designs while as well ensuring the vehicles meet performance goals. Simultaneously, the development of hypersonic vehicles is justified by their potential to drastically reduce travel times, especially for business and emergency applications. This increasing need for cutting-edge hypersonic research highlights the wider strategic benefits that go beyond economic and environmental considerations. With increased feasibility, there is a concerted push for continuous research into waveriders, a type of HGV, and other advanced aerodynamic configurations to improve the performance and efficiency of hypersonic flight systems (LIU J.; DING, 2014) and (BIN X.; ZHONGKE, 2015).

The pioneer in the field of hypersonic flight was the development of Hypersonic

Technology Vehicles (HTV), as part of **The Falcon Hypersonic Technology Program**, developed by DARPA and the U.S. Air Force, which is focused on advancing hypersonic flight technologies to create reusable, high-speed vehicles capable of reaching Mach 10(WALKER S.H.; RODGERS, 2012). The program includes the development of a Small Launch Vehicle (SLV) and a HTV, designed to test essential technologies required for hypersonic flight, in particular for HCV with global reach. Through a series of increasingly challenging flight tests, the HTV program seeks to validate technologies like aerodynamics, thermal management, and guidance and control. The HTV series will also refine these technologies to improve lift-to-drag ratios, thermal protection systems, and long-duration flight capabilities which are key characteristics of HGV, capable of maneuvering during reentry into the atmosphere. The program also incorporates initiatives like the **HyCAUSE** program, which focuses on scramjet and turbojet propulsion systems, contributing to the development of a fully reusable hypersonic vehicle designed to reach Mach 10. These efforts are paving the way for the future of hypersonic flight and the potential operational deployment of the **North American Aviation X-15** (JERKINS, 2012). The program began in 1954 and featured test flights from 1959 onward. There were 3 test aircraft manufactured, participating in 199 flights in total. They were dropped at high altitudes from a modified B-52 aircraft, after which their own engines would start, and the flight-testing phase could begin. The X-15 established the foundation for the current understanding of hypersonic flight dynamics and the efficiency of control systems.

Figure 2 – The X-15 No.2 (56-6671) launches away from the B-52 mothership with its rocket engine ignited.

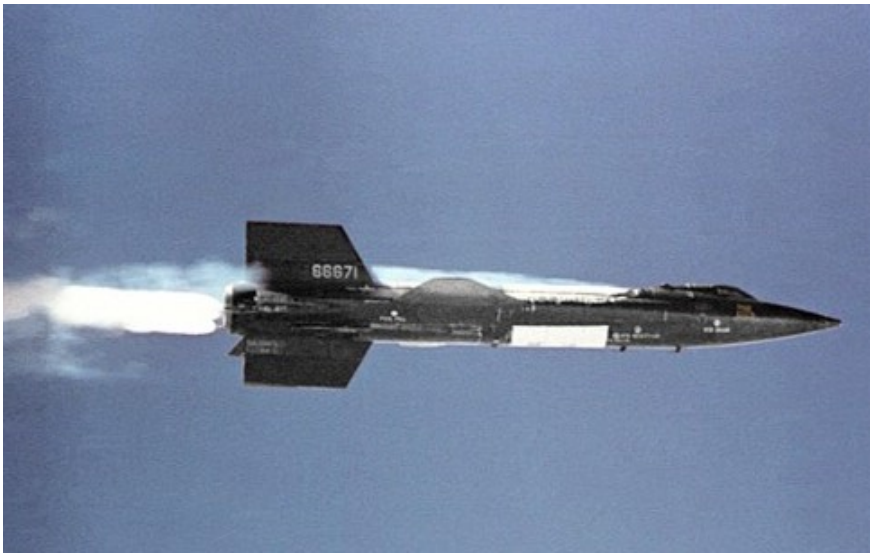

Source: NASA.

While not fundamentally different, the application of hypersonic technologies extends beyond military use, influencing projects like the **Space Launch System (SLS)** (SZIROCZAK D.; SMITH, 2016). In contrast to traditional space access technology, the

SLS can reach, operate in, and return from orbit without expending the vehicle. The Space Shuttle program, which operated from 1981 to 2011, was a major part of this endeavor. Although it did not fully achieve its initial objectives, especially with regard to cost and turnaround time, it did show that spacecraft could be partially reused. The SLS intends to expand on these lessons with further advancements to overcome the limitations seen in the Shuttle program. Contemporary projects, such as the **Reusable Orbiter SL-12** and NASA's **X-37**, carry on the exploration of reusable systems in space exploration.

Figure 3 – Space Shuttle Discovery (STS-31) comes in for a landing on April 29, 1990.

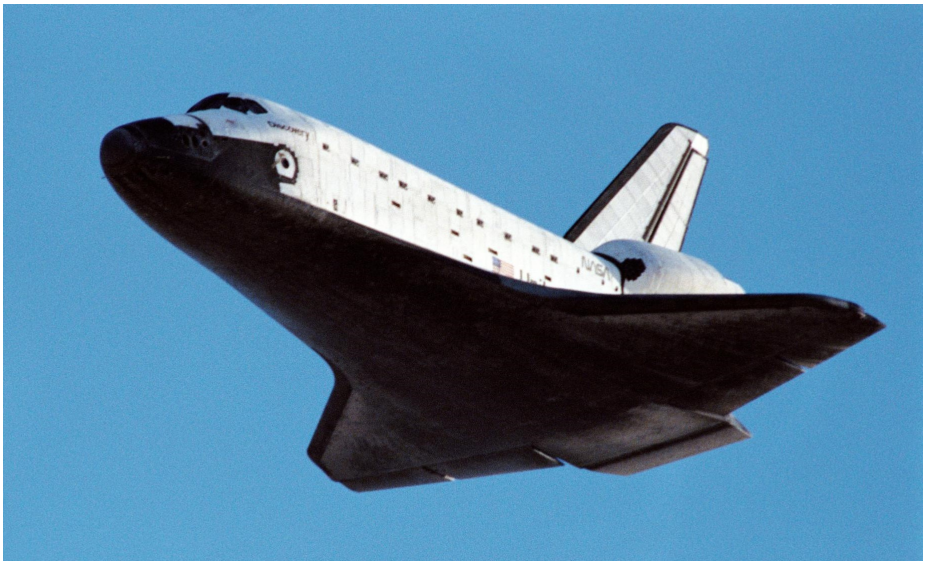

Source: NASA.

The Hypersonic Transport Technology (HTT) system seeks to revolutionize air travel, whereas the Space Launch System and related technologies focus on space missions. The HTT, which operates at speeds above Mach 5, utilizes hypersonic technology to drastically cut down travel times across the globe. Although no operational hypersonic transport vehicles have been constructed or flown to date, there are projects in the testing stage. These vehicles face many challenges, especially due to developing technology and high investment costs. Despite these obstacles, the potential to reduce travel times is still a compelling reason to continue investing in hypersonic transport systems. This work focuses on one of these proposals: **the waveriders**.

Waveriders are a particular class of hypersonic vehicles known for their unique aerodynamic design that exploits shock waves to enhance lift and flight efficiency. These vehicles frequently function as gliders, maintaining high speeds without constant propulsion, and achieve **high lift-to-drag ratios**, a crucial metric for efficient hypersonic travel (HUANG W.; MA, 2011). To date, the Boeing X-51 is the only waverider configuration that has successfully demonstrated flight. However, a major limitation of waveriders is that their lift enhancement is optimized for a certain Mach number and altitude combination,

making them less efficient outside those conditions. Despite this, waveriders have no inherent aerodynamic disadvantage over traditional lifting body vehicles. In fact, if correctly aligned, their attached shock wave can also be used for ram compression, benefiting airbreathing propulsion systems. The X-51, powered by a scramjet engine, exemplifies this potential and is being developed through a collaborative effort between the USAF, DARPA, NASA, Boeing, and Pratt & Whitney Rocketdyne (BOEING, 2005). Their ability to utilize attached shock waves makes them especially efficient during the unpowered phase of flight. Over the past five decades, researchers have broadened the design space of waveriders by exploring different basic flow fields from which their shapes can be generated, aiming to improve their aerodynamic and volumetric efficiency. Understanding the behavior of these vehicles under various flight conditions has become increasingly dependent on sophisticated simulation tools, most notably **Computational Fluid Dynamics (CFD)**, which allows for in-depth analysis of complex hypersonic flow fields.

CFD is a powerful tool used to analyze and simulate fluid flow behavior in complex systems, such as the aerodynamic performance of hypersonic vehicles. By using **numerical methods** and **algorithms**, CFD enables the study of fluid dynamics in conditions where conventional analytical methods become impractical, espacially in high-speed regimes like hypersonic flight. In CFD simulations, the fluid flow around an object is broken down into smaller, more manageable elements, and the governing equations of fluid motion are solved iteratively to predict different fluid properties, like velocity, pressure, and temperature distribution.

In aeronautics, CFD has proven to be indispensable for the analysis of hypersonic flows, particularly when evaluating aerodynamic performance under both **on-design** and **off-design conditions**. Off-design conditions, which include changes in Mach number and the orientation of the incoming flow, are difficult to calculate analytically, but CFD offers the only useful way to study these properties. CFD simulations allow for the evaluation of aerodynamic performance not only under ideal conditions but also in **real-world operating scenarios** where flight conditions can change. Furthermore, CFD simulations are essential for the validation of the hypersonic vehicles design and investigating how various configurations, such as compression surfaces and variable shock angles, impact aerodynamic performance. This method is crucial for optimizing the design efficiency for hypersonic flight conditions and refining configurations for off-design flight phases.

The present work, seeks to provide valuable insights into the understanding of **Waverider configurations**. By focusing on the aerodynamic aspects, the aim is to contribute to the long term development of improved design methodologies for future hypersonic vehicles.

This study expands on earlier research, particularly the work of Rolando (GUZMÁN-BOHÓRQUEZ, 2024), which showed great promise in the field of hypersonic vehicle design

due to its optimized waverider geometry. Even though the original intention of this project was to replicate and extend those simulations using a different computational framework, the scope has been adapted because of practical considerations. Instead of directly simulating the optimized geometry, this work now focuses on a **wedge configuration**. This wedge can be considered the most fundamental representation of a waverider, serving as a baseline for understanding aerodynamic behavior before moving on to more complex, fully optimized designs

By adopting this approach, the study provides a controlled environment to asses the numerical setup, computational parameters, along with boundary conditions. Establishing this base is important to ensure that future simulations of optimized geometries are both reliable and reproducible. On the other hand, because this work scales the wedge toward the reference dimensions of Rolando's optimized model, it maintains a direct connection with previous research and enables meaningful comparisons and continuity between studies.

1.1 Objectives

Understanding this work as the groundwork for future studies, the goals of this project can be listed as follows.

1. **Establish a simplified aerodynamic model,**the wedge configuration serves as the most fundamental representation of a waverider. This provides a controlled baseline for analysis.

2. **Assessment of the computational framework,** testing numerical schemes, mesh strategies, and boundary conditions. This ensures reliability and reproducibility of future simulations.

3. **Continuity with previous research,** by scaling the wedge geometry according to the reference dimensions of Rolando's waverider model.

4. **Analyze the aerodynamic behavior of a wedge** under hypersonic flow conditions, including flow structures, pressure distribution, along with lift and drag characteristics.

5. **Establish methodological foundation** for future research efforts, contributing to the broader development of hypersonic vehicle technologies.

2 LITERATURE REVIEW

At high-speed flight conditions, the lift-to-drag ratio (L/D) of a vehicle tends to decrease as the freestream Mach number increases. This phenomenon is a consequence of the intensification of shock waves and the subsequent rise in wave drag at high speeds. For hypersonic vehicles operating at high Mach numbers, the L/D ratio becomes relatively low, which could pose a challenge for the development of future atmospheric hypersonic vehicles. However, waveriders, a specific class of hypersonic vehicles, offer a solution by attaching the shock wave along its leading edge. This design enables higher L/D values compared to other generic vehicles, making waveriders a promising configuration for hypersonic flight (ANDERSON, 1984).

Figure 4 – Comparison of waverider and generic hypersonic shock wave configurations.

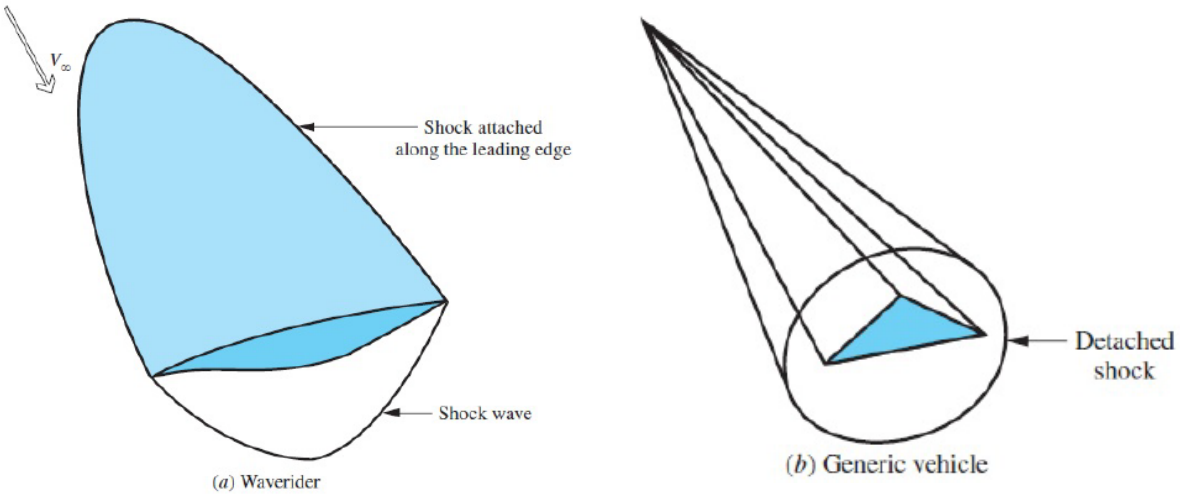

Source: (ANDERSON, 1984).

2.1 History and Development of Waveriders

The term "Waverider" was coined by Dr. John Seddon (PIKE, 1990) to describe a family of wing shapes developed by Prof. Terence Nonweiler at Queen's University, Belfast and first described in print in 1959 (NONWEILER, 1959). These wings are designed to generate a shockwave attached to their leading edges, which creates lift by utilizing high-pressure areas beneath the vehicle. Nonweiler's original design featured a folded delta wing shape (Figure 5), later known as the Caret Wing. This idea emerged during his time as a consultant on manned spaceflight at Armstrong Whitworth Aircraft following the launch of Sputnik 1 (GATLAND, 1959). Nonweiler's work on the Pyramid Wing led to the development of a vehicle designed with a hollow, conical underside which allowed the shockwave to remain attached to the leading edge. Due to limited computational

resources, Nonweiler developed the Waverider by applying origami techniques to simplify the shockwave calculations.

Figure 5 – Nonweiler designs for single and double-shock wings.

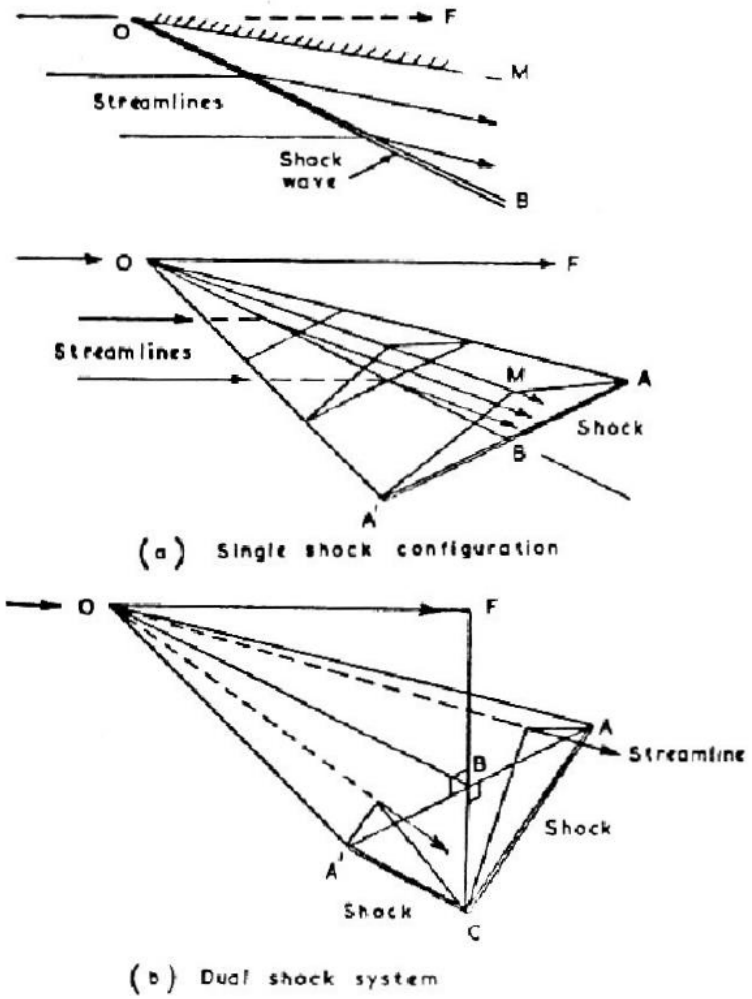

Source: (NONWEILER, 1959).

The Waverider concept gained significant attention, which encouraged Nonweiler to further develop the idea in a more focused paper (NONWEILER, 1962). This study earned him the Royal Aeronautical Society's Gold Medal and introduced a new flight principle that made a lasting impact on aerospace research. The Royal Aircraft Establishment (RAE) and other institutions investigated the use of Waveriders for Mach 6 aircraft, including airliners and military projects with testing focused on improving stability and lift-to-drag ratios The airliner design gradually evolved into one featuring a "Gothic arch" shaped cavity, achieving high L/D. These efforts continued into the 1970s with more refined models and wind tunnel experiments (KÜCHEMAN, 1978).

In 1980, Dr. Maurice Rasmussen expanded on the work of Terence Nonweiler, utilizing hypersonic small-disturbance theory to design waveriders based on shockwaves over

circular and elliptic cones (RASMUSSEN, 1980). Rasmussen applied the classic calculus of variations to optimize the waverider shapes, leveraging the inviscid flow properties. His work led to the development of an "idealized Waverider" that generated a conical shockwave, enhancing aerodynamic efficiency. This concept was further explored with 3D computational studies at the University of Maryland around 1982, which significantly advanced the understanding of waverider performance. Dr. James Randolph from the Jet Propulsion Laboratory (JPL) also contributed by exploring waverider designs for the Starprobe mission (MACROLAND A.D.; RANDOLPH, 1990), which later became the Solar Probe, aimed at utilizing aerogravity maneuvers to reach the Sun.

At the 1990 First International Hypersonic Waverider Symposium, Dr. Alfred J. Eggers proposed expanding the term "Waverider" to include any vehicle generating attached shockwaves, which led to debates about its definition and scope (EGGERS A.J.; ASHLEY, 1990) and (BAUER S.X.S.; COVELL, 1990). As computational capabilities improved, waveriders were tested in various high-speed environments, including NASA's SOAREX program and other hypersonic experiments (NASA, 1998). These tests confirmed the feasibility of waveriders for suborbital and orbital missions, demonstrating their efficient operation at hypersonic speeds. By the late 1990s, waveriders had been incorporated into advanced projects, such as the X-51 scramjet program, further solidifying their role in hypersonic flight.

In early 2003, the U.S. military launched the Endothermically Fueled Scramjet Engine Flight Demonstrator (EFSEFD), with test flights starting in 2006. The X-51, part of the EFSEFD program, featured a single scramjet engine with a fixed-geometry inlet (USAF, 2011). In 2004, the U.S. Air Force selected Pratt & Whitney and Boeing to develop the Scramjet Engine Demonstrator Waverider (SED-WR), which would launch from a B-52. The first X-51 test flight occurred in December 2009, and in May 2010, it successfully flew for 140 seconds at Mach 4.5. After some challenges, the final test in May 2013 was a success, reaching Mach 5.1. The program highlighted the potential of scramjet-powered vehicles for military applications but also raised questions about the broader uses of Waverider technology (NORRIS G., 2012).

Figure 6 – An X-51,A Waverider hypersonic flight test vehicle is uploaded to an Air Force Flight Test Center B-52 for fit testing at Edwards Air Force Base on July 17, 2009.

Source: Air Force.

2.2 Design Methodology

The core of the Waverider design methodology lies in shaping the streamlines that form the vehicle's compression-stream surface. Both the shape and pressure distribution of these streamlines are dictated by the basic flow field. The design process involves defining and solving the basic flow field, tracing a set of streamlines within this field, and then lofting these streamlines to generate the vehicle's compression-stream Surface (DING F.; LIU, 2017). Therefore, we can classify the basic stream flows as either two-dimensional or three-dimensional, and further categorize them as planar or axisymmetric.

The concept of waveriders, introduced by Nonweiler (NONWEILER, 1962), begins with simple three-dimensional lifting bodies derived from two-dimensional planar flow field, wedge flows. The wedge-derived waverider, although of limited practical value due to its low volumetric efficiency, set the stage for future hypersonic vehicle research. The simplest of these configurations are the caret waveriders, characterized by their flat surfaces and sharp edges. The caret waverider is also referred to as the V-shaped wing, with studies indicating that at supersonic or hypersonic speeds, the V-shaped wing proves more efficient than an equivalent planar triangular wing (OSTAPENKO, 1993). This is because it has a shock attached to the leading edges, resulting in a higher L/D ratio.

Figure 7 – Nonweiler or Caret wing.

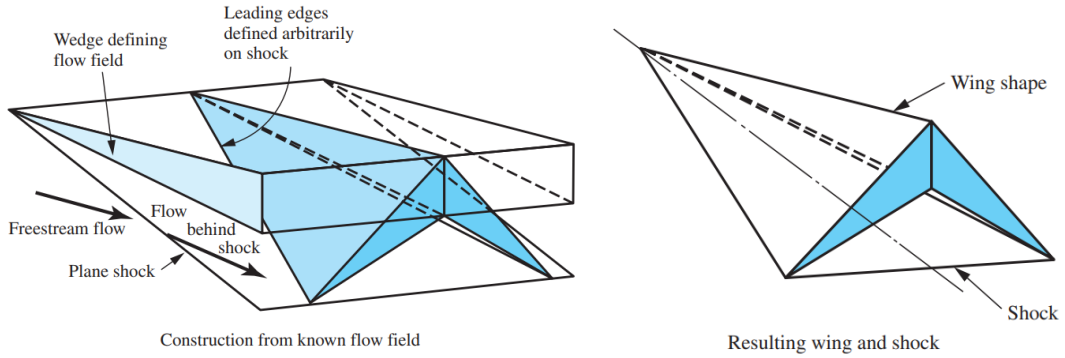

Source: (NONWEILER, 1962).

While effective in idealized, inviscid theory, these sharp edges may present challenges due to viscous and heating effects. To overcome this, more advanced waverider configurations use curved surfaces, which are derived from inviscid two-dimensional axisymmetric basic flow fields (RASMUSSEN, 1980). Based on the shape of the flow field it can be differentiated into conical, curved conical or internal conical.

The conical flow field is the most widely used basic flow field for waveriders due to its simplicity and efficiency. These cone-derived waveriders feature attached shock waves and smooth curvatures, offering improved aerodynamic properties (JONES J.G.; MOORE, 1968). They have a better volumetric efficiency than wedge-derived waveriders, thanks to concave streamlines that are closer to the shock wave.

The curved conical flow field over minimum drag bodies, helps ensure a fully attached shock wave while maintaining supersonic flow conditions (CORDA, 1988). Waveriders based on this curved flow field had higher L/D ratios than those based on the traditional cone-derived flows (MANGIN B.; BENAY, 2006). However, the total volume of these waveriders is higher, which could be a disadvantage in certain design contexts. Later studies confirmed that waveriders derived from these flows showed better performance in volumetric efficiency compared to wedge-derived waveriders and better air compression ability of the engine in comparison to the cone-derived waverider; resulting in a much better suited configuration for airframe-engine integration (HE X.; LE, 2009).

The internal conical flow field develops a class of waveriders termed osculating inward turning cone waveriders. These designs exhibit high compression capabilities, improved pressure recovery, and enhanced lift coefficients as well as offer the added advantage of reduced flow spillage and lower heat flux (MOLDER, 1967). They are particularly useful for airframe-engine integration in hypersonic vehicle designs.

Figure 8 – General cone-derived waverider.

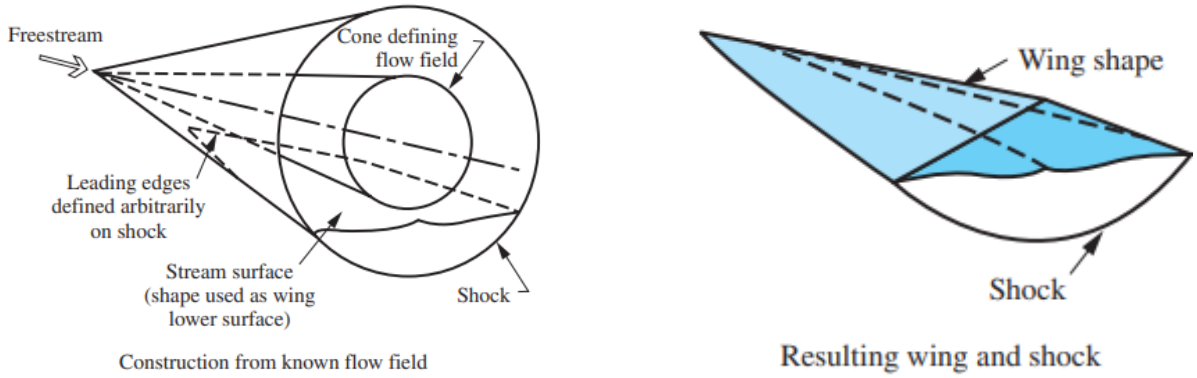

Source: (ANDERSON, 1984).

Extending waverider design beyond axisymmetric flows to three-dimensional inviscid flow fields has proven to significantly expand the aerodynamic performance possibilities by offering more diverse and efficient configurations (HUANG W.; MA, 2011). This approach allows for the optimization of parameters such as L/D ratio and volumetric efficiency. As early as 1980, Rasmussen was the first to explore the use of quasi-cone flows, demonstrating the potential of 3D inviscid flow fields in enhancing waverider designs (RASMUSSEN, 1980) The results highlighted the fundamental impact of selecting the appropriate flow field geometry on the overall performance, emphasizing the need for continued exploration of 3D configurations in hypersonic vehicle design (PENG B.; BINGYAN, 2016).

Figure 9 – View of 3D waverider design.

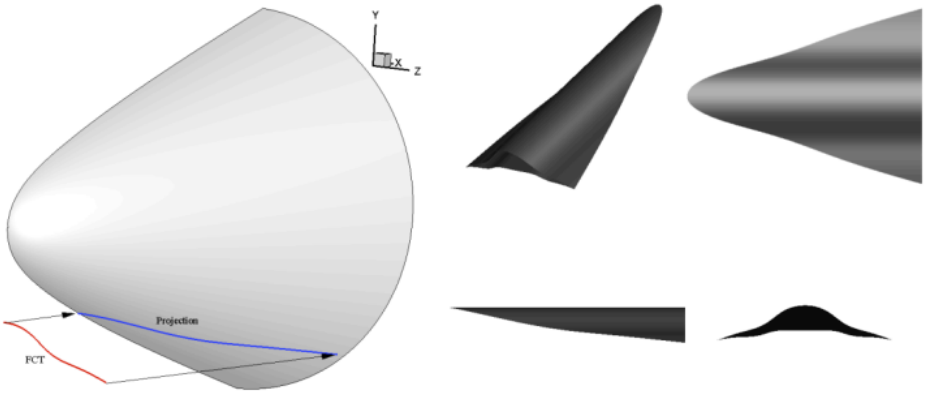

Source: (PENG B.; BINGYAN, 2016).

2.3 Waverider Configurations

To bring the concept of waveriders into practical use, the main challenge lies in their high dependency on Mach number. These vehicles are designed and optimized to operate efficiently within a specific Mach range. However, this is unrealistic in practical scenarios

where takeoff, landing, and in-flight maneuvers require operating at various speeds. As such, numerous studies have been dedicated to exploring potential configurations that can handle a wide range of flight speeds. The most relevant approaches include combined wide-speed range designs, variable Mach number configurations, vortex lift models, dual systems, and morphing technologies.

The combined wide-speed range waverider configuration refers to a design approach where multiple waveriders, each optimized for different Mach numbers, are combined either directly or through connecting segments. Key challenges include the optimization of connection sections and ensuring consistent aerodynamic behavior across various flight conditions. An example of this type of configuration is a proposed method combining low-speed and hypersonic waveriders using osculating cone theory (WANG, 2009) Across Mach 0.3 to 7.0, a lift-to-drag ratio above 3.5 is achieved. Alternatively, the Tandem configuration studies how the length of the connection section, fore-body thickness, and afterbody width affects aerodynamic performance (LI S.; LUO, 2013) The connection section length had the most significant impact. The Parallel wide-speed range waverider, combining high and low Mach waveriders in parallel, improves L/D ratios, particularly in hypersonic speeds (LI S., 2014). The star-body waverider, which involves combining multiple wedge-derived waveriders, was another design explored, reducing drag but suffering from shock detachment at off-design Mach numbers (GONOR A.L.; KAZAKIV, 1971). However, issues such as shock detachment at non-design Mach numbers and lack of lift or side force at zero angle of attack limit its effectiveness.

Figure 10 – Combined wide-speed range waverider configuration examples.

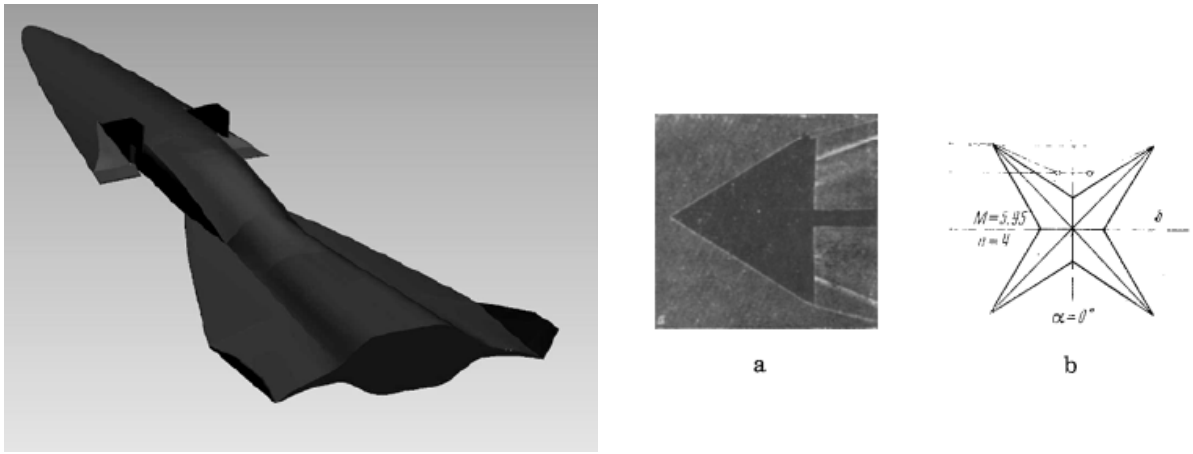

Source: (GONOR A.L.; KAZAKIV, 1971).

The variable Mach number configuration is based on adapting the waverider shape to accommodate variable Mach numbers, improving aerodynamic performance at different flight speeds. Using streamline tracing and lofting methods, the waverider's geometry is modified to balance aerodynamic performance from subsonic to hypersonic regimes.

To achieve this, the conical-derived variable Mach number waverider is introduced using streamline-tracing to allocate different Mach numbers across lateral areas of the lower surface (ZHANG T.; WANG, 2017). Another approach is the use of osculating cone theory, improving aerodynamic performance by enhancing the lift-to-drag ratio over the entire flight profile compared to traditional designs (ZHAO Z.; HUANG, 2018).

Figure 11 – Geometric models of conical-derived and osculating cone variable Mach number waveriders.

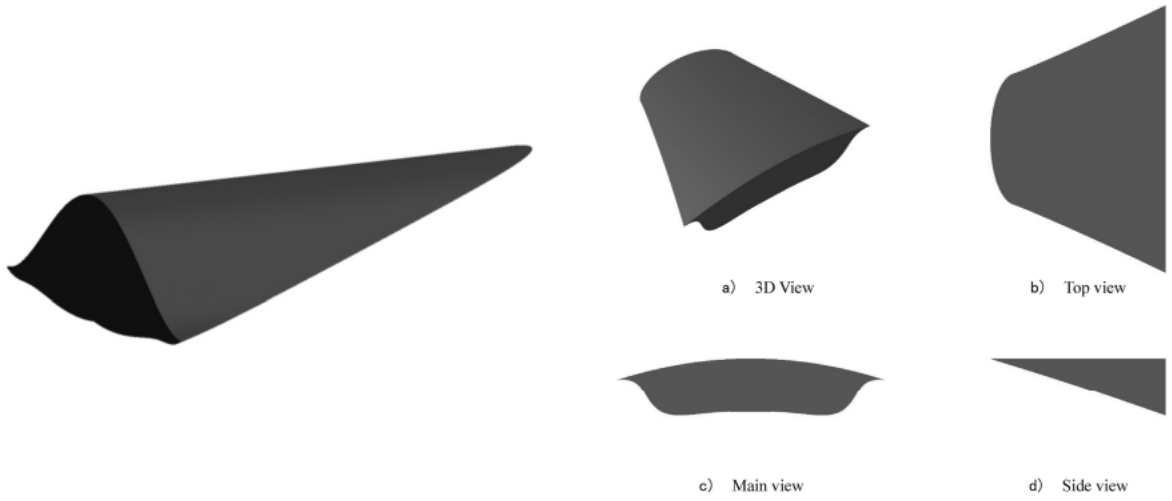

Source: (ZHANG T.; WANG, 2017) and (ZHAO Z.; HUANG, 2018).

The vortex lift waverider leverages vortex flow to enhance lift at lower Mach numbers by employing swept-back wing designs and generating leading-edge vortices (RODI, 2012). This design can increase the lift-to-drag ratio, especially in transonic and supersonic regimes, while minimizing drag in low-speed conditions. Two methods to enhance vortex lift include increasing the angle of attack or introducing expansion on the leeward side.

Figure 12 – A sketch of vortex lift waverider features at high angles of attack.

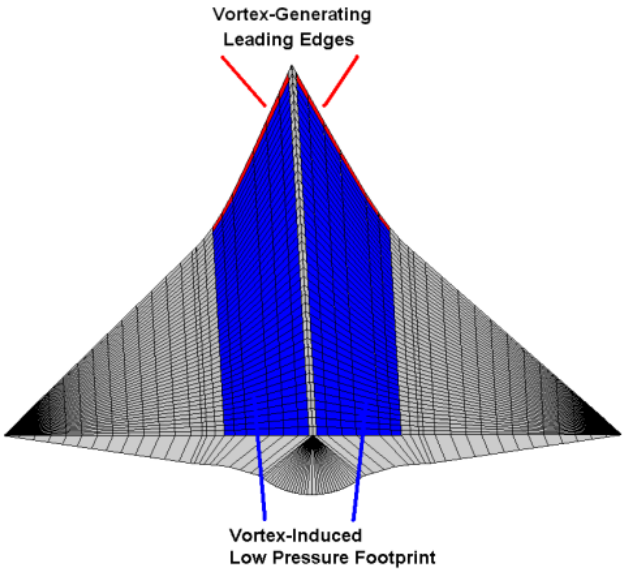

Source: (RODI, 2012).

The gliding–cruising dual waverider is a novel design concept which focuses on a hypersonic vehicle that operates efficiently during both the gliding and cruising phases (LIU J.; DING, 2014). In the gliding phase, the vehicle rides on the shock wave at the designated gliding Mach number, with the inlet shroud acting as the waverider's compression surface, facilitating smooth air compression and reducing drag. During the cruising phase, the vehicle transitions to a lower cruising Mach number, and the inlet shroud is either jettisoned or retracted. In this phase, the fore-body of the vehicle serves as the compression surface, optimizing aerodynamics for efficient sustained flight at high speeds.

Figure 13 – Geometric model of the gliding–cruising dual waverider test case.

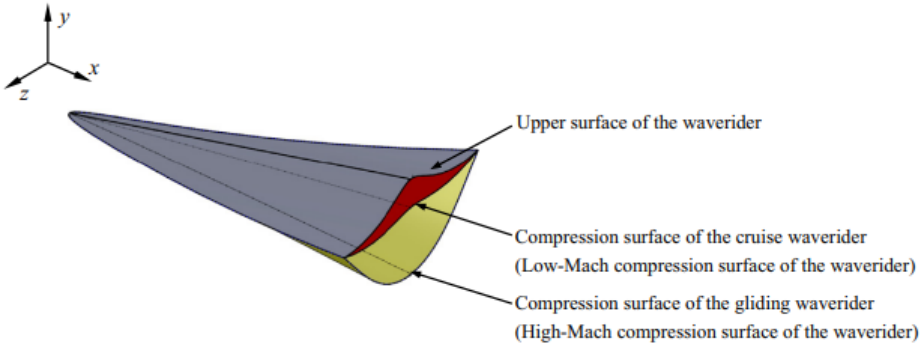

Source: (LIU J.; DING, 2014).

Morphing waveriders use adaptive materials and actuators to adjust the vehicle's shape in flight. The design employs actuated surfaces that adjust the waverider's shape, maintaining efficient shockwave attachment and aerodynamic performance from Mach 5

to subsonic speeds (RODI, 2016). This technology bridges the gap between high-speed and low-speed flight, enhancing the vehicle's overall flight envelope and stability. This technology is considered key for next-generation aircraft.

Figure 14 – Example Mach 5 and Mach 10 morphing waverider for 10 km fixed altitude.

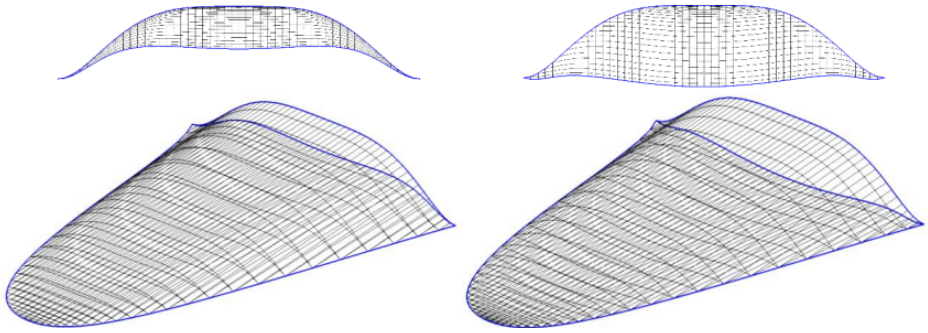

Source: (RODI, 2016).

3 METHODOLOGY

3.1 Model description: GMSH

This study serves as a continuation of previous research on (GUZMÁN-BOHÓRQUEZ, 2024), but with a revised scope. The current work focuses on a simplified wedge configuration rather than directly simulating the optimized waverider geometry developed in earlier studies. This wedge is designed to be the most basic type of waverider, maintaining an equivalent overall length, span, and height as the optimized model while simplifying the geometry to its most basic aerodynamic representation.

The motivation behind this approach lies in the need to establish a solid computational framework before dealing with more complex geometries. The study creates a controlled test case for the simulation of the wedge, allowing for the systematic verification of flow characteristics, boundary conditions, and numerical settings. The configuration serves as a useful first step toward replicating and building upon those results, even though it lacks the geometric refinements added during the multi-objective optimization of aerodynamic efficiency (lift-to-drag ratio, L/D) and volumetric capacity (V) (SILVA, 2021).

This primitive wedge lacks blunt-leading-edge treatments and other thermal protection adaptations, in contrast to the original optimized waverider (MORAN J. H.; MCQUELLIN, 2023). Instead, it represents an idealized geometry that is used as a starting point for aerodynamic analysis under hypersonic flow conditions. Its simplicity guarantees that, without the need for extra design variables, the simulation results can be directly attributed to the basic flow–geometry interactions.

In the following subsections, the necessary geometric and meshing specifications used in the numerical simulations are presented developed using the software **GMSH**. GMSH is an open-source 3D finite element mesh generator with a built-in CAD engine and post-processor. These details will provide the necessary foundation for the subsequent aerodynamic analysis and performance evaluation of this configuration in order to build a methodological pathway toward future analyses of optimized waverider configurations.

3.1.1 Geometry

To understand the geometry used, it is necessary to assign values to the reference length, span and height and therefore the internal volume. The reference length is defined as the straight-line distance along the x-axis between the most distant points on the leading and trailing edges, later used by the simulation software to calculate the corresponding coefficients. The exact values of these measures are not provided due to confidentiality,

they correspond to equivalent dimensions from the optimized waverider geometry, which can be used for comparison.

The model has been defined through text files written in GMSH's own scripting language, .geo file, which provides a versatile and efficient way of creating and modifying geometric configurations. GMSH allows for the precise definition of geometries, including the application of boundary conditions, material properties, and mesh generation.

	Symbol	**Value**	**Units**
Reference length	L	1	m
Span	b	0.37	m
Height	z	0.17	m
Internal volume	V	0.03145	m^3
Wetted Area	S_{wetted}	0.47414	m^2

Table 1 – Geometry data.

Due to the symmetry of the problem, it is only necessary to represent one half of the wedge. This is possible because aerodynamic models often exhibit mirror symmetry, particularly those with a simple geometric shape like a wedge. This means that the flow properties, such as pressure distribution and velocity fields are the same on both sides of the centerline. The computational domain is shrunk by taking advantage of this symmetry, which results in considerable computational resource savings without sacrificing simulation accuracy. Consequently, only one half of the wedge is visible in Figure 15.

Figure 15 – Wedge general view.

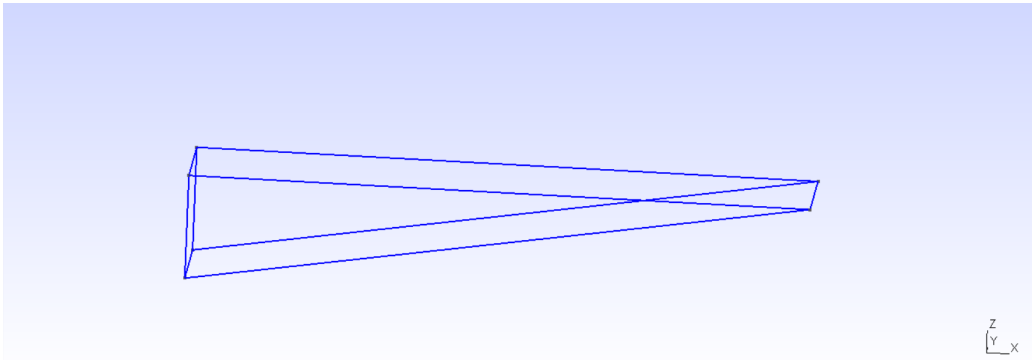

Source: Author.

3.1.2 Mesh configuration

In this study, a **tetrahedral unstructured mesh** has been employed created directly from the .geo file using (Geuzaine, C.; Remacle, J., 2025), just like the geometry. The mesh covers the control volume over which the flow equations will be solved, therefore it does not include the wedge itself but rather the surrounding air. This approach guarantees

that the computational domain captures the flow behavior around the geometry, providing a detailed representation of the aerodynamic interactions between the wedge and the surrounding fluid.

When working with geometries that need local refinement or have irregular shapes, unstructured meshes are especially useful. These meshes allow for the use of non-aligned cells that can adjust to the geometry, in contrast to structured meshes where the grid has a regular pattern. This flexibility comes at the expense of increased computational demand, because the mesh generation and solver operations require more complex algorithms. By using an unstructured mesh, it becomes possible to define areas with finer mesh density, ensuring a more accurate representation of the flow features in critical zones and in regions where higher resolution is required.

Tetrahedral meshes consist of four-sided elements that allow for a fine mesh distribution in the areas of interest while maintaining the overall flexibility of the unstructured mesh. Since tetrahedral meshes can closely resemble the surface of the model, they are especially helpful for simulating flows over complex geometries and uneven surfaces. Despite their computational intensity, tetrahedral meshes provide the necessary resolution for capturing important aerodynamic features around the wedge geometry, ensuring an accurate flow representation.

Figure 16 – 3D Fluid meshing.

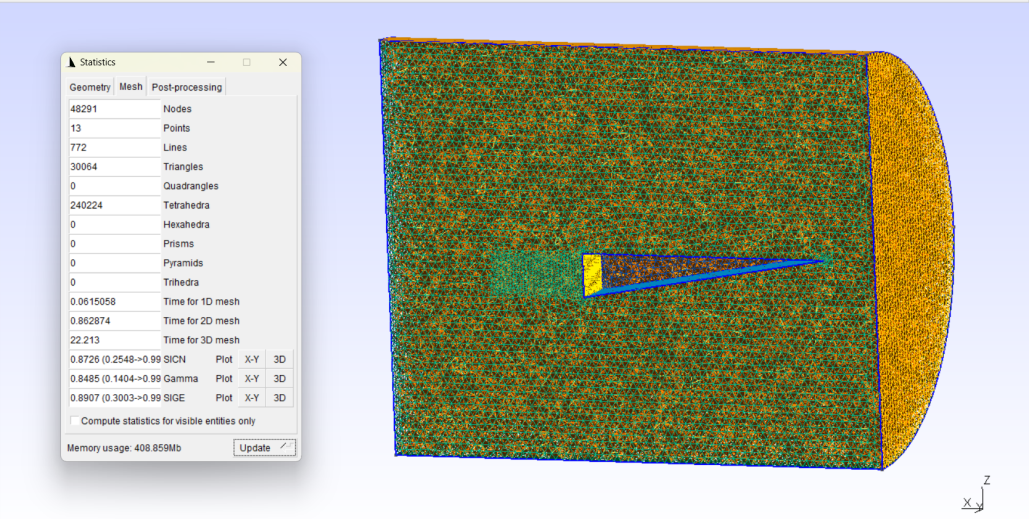

Source: Author.

The control volume has a cylindrical shape and, since high resolution is not needed, a coarser mesh has been applied. The 2D mesh definition is shown in Figure 17, where the shape and boundaries of the control volume are represented.

Figure 17 – Control Volume's surface grid.

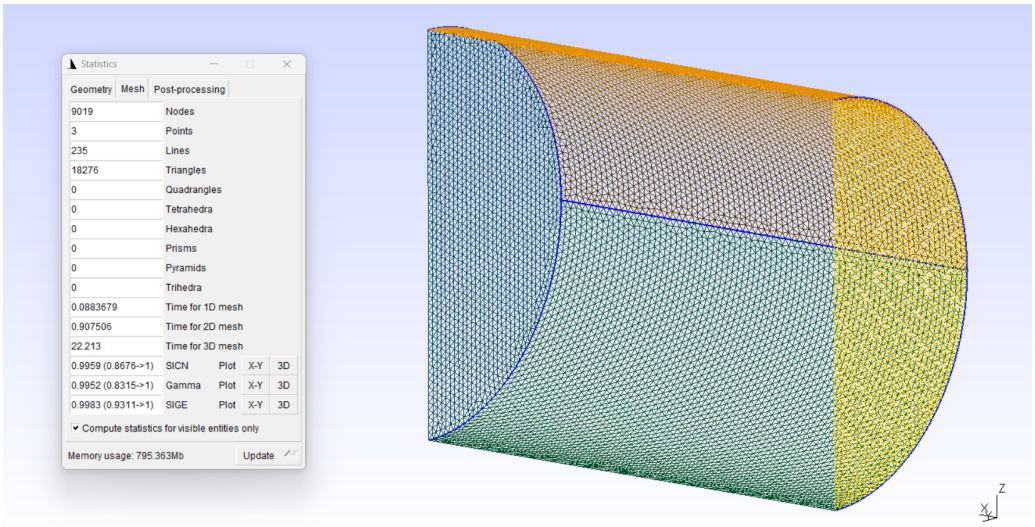

Source: Author.

Regarding the wedge surface, the meshing is more complex. A higher resolution is required over the wetted surface, which corresponds to the boundary layer, as well as an increased refinement at the leading and trailing edges. This is achieved using the *MathEval* command for surface refinement and the *Threshold* command for edge refinement, ensuring that the mesh is finer where it is most needed to accurately capture the aerodynamic features.

Figure 18 – Wedge's surface grid.

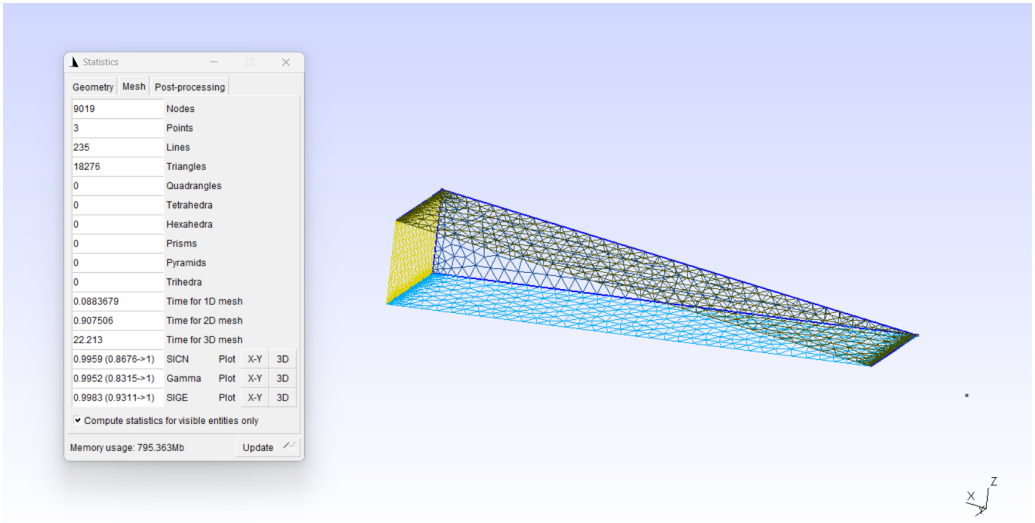

Source: Author.

Figure 19 – Detailed leading edge meshing.

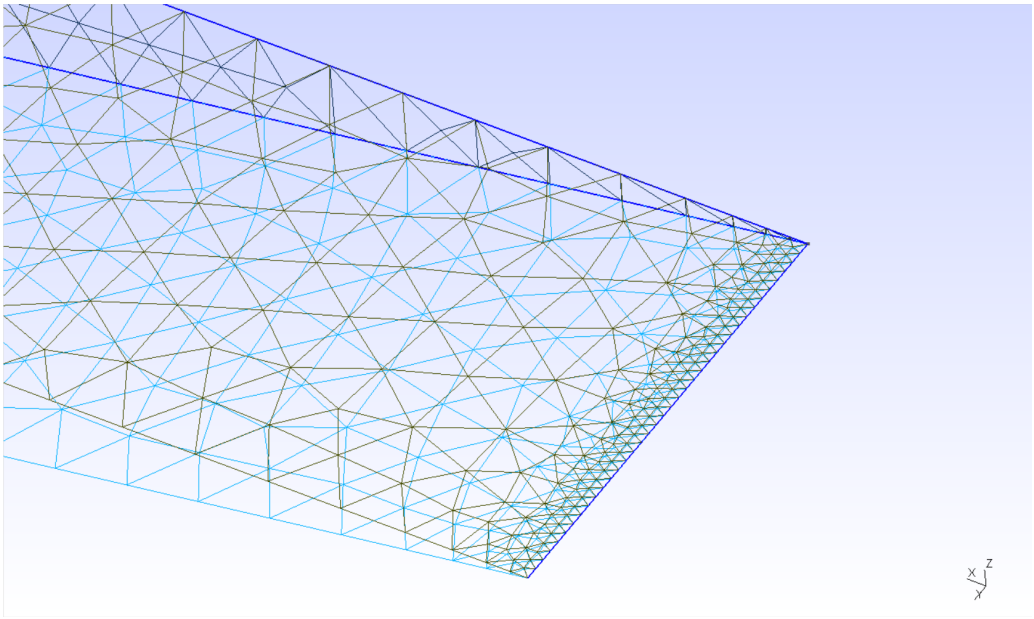

Source: Author.

Figure 20 – Detailed trailing edge meshing.

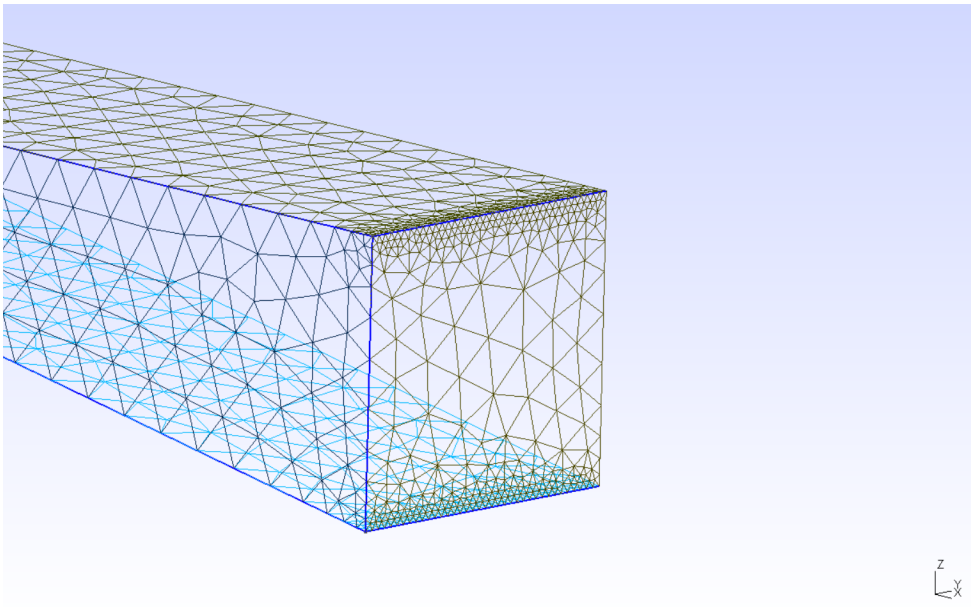

Source: Author.

Finally, to capture the wake generated by the wedge, a distinct mesh is defined for this region using the *Box* command. This ensures that the mesh is properly refined in the wake area, allowing for an accurate representation of the flow structure downstream of the wedge.

Figure 21 – Detailed wake meshing.

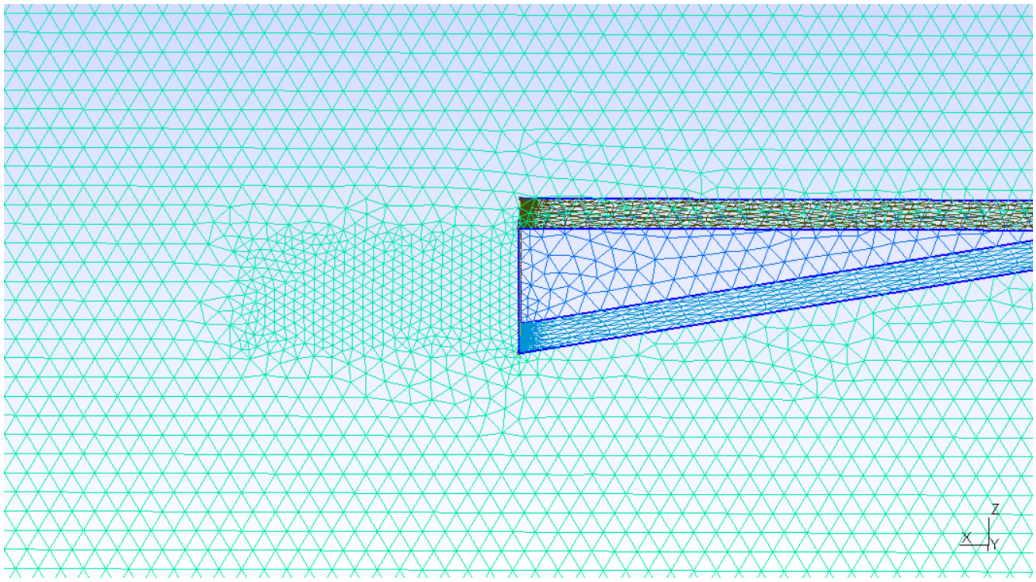

Source: Author.

With all these elements, the mesh composition is defined, and the final step is to declare the surfaces that constitute the boundary condition. These are essential for correctly applying symmetry, the far-field domain, and the model's walls in the simulation, ensuring accurate boundary interactions and flow behavior during the computation.

Figure 22 – Definition of Boundary Conditions.

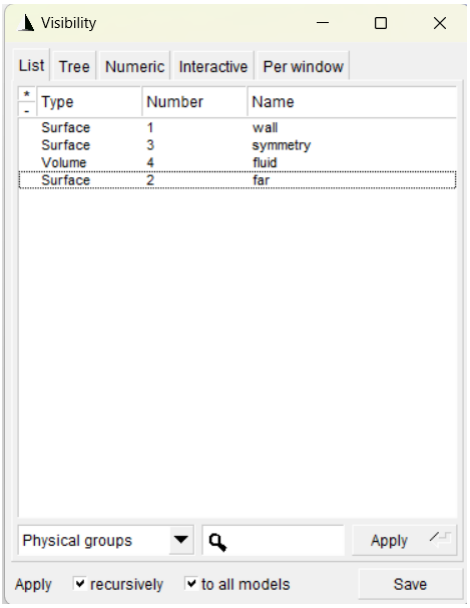

Source: Author.

For computational fluid dynamics simulations to be accurate and stable, mesh quality is a crucial component. By reducing errors and enhancing convergence, a high-

quality mesh guarantees that the numerical solution accurately captures the physical problem. One of the key metrics used to assess mesh quality is the **gamma coefficient** (γ), which compares the radius of the inscribed sphere (the largest sphere that fits within the mesh element) to the radius of the circumscribed sphere (the smallest sphere that encloses the element). A higher value of γ indicates a well-shaped element with a near-circular or equiangular shape. In this study, the mesh has been designed to achieve high gamma values, indicating that the elements are of high quality and suitable for accurately capturing the flow characteristics around the wedge geometry.

Figure 23 – Distribution of Mesh Elements by Gamma Coefficient.

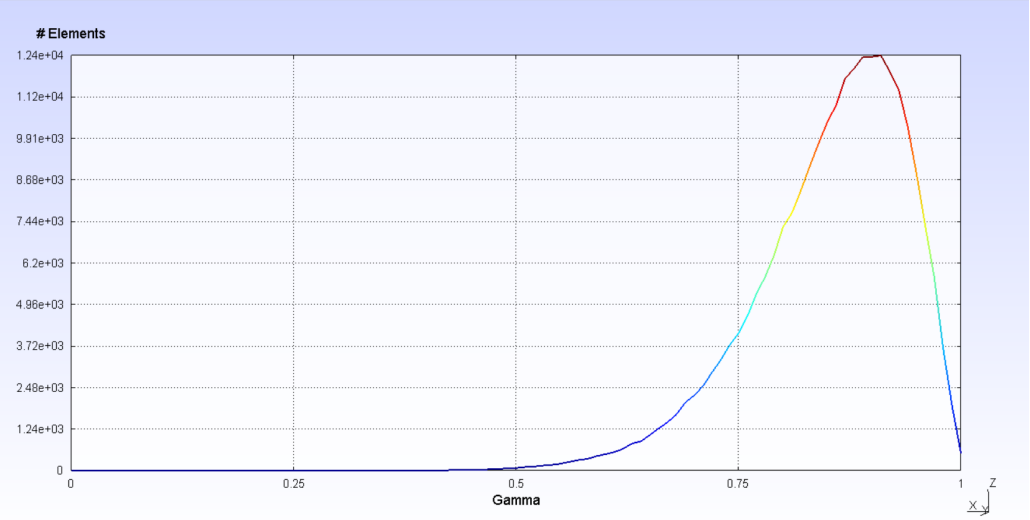

Source: Author.

The **SICN (Signed Inverse Condition Number)** is another widely used metrics for assessing grid quality. This measure refers to the numerical condition of the grid elements, where values close to 1 indicate good quality grid elements, and values approaching 0 suggest that the grid element is degenerate or highly distorted

Figure 24 – Distribution of Mesh Elements by SICN.

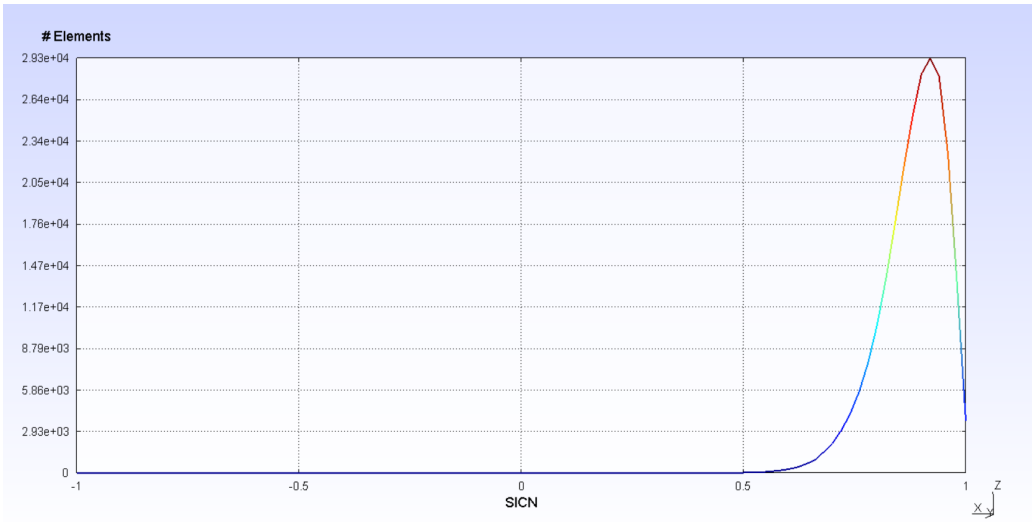

Source: Author.

Another important mesh quality metric is **SIGE (Signed Inverse error on the Gradient)**, which evaluates the accuracy of the gradient estimation within the mesh. SIGE quantifies the inverse of the error in the gradient approximation at each finite element. A high SIGE value indicates that the mesh accurately captures the gradients of the field variables, such as pressure and velocity, with minimal error. This is crucial for ensuring the accuracy of the simulation, particularly in regions with high gradients, such as shock waves or boundary layers.

Figure 25 – Distribution of Mesh Elements by SIGE.

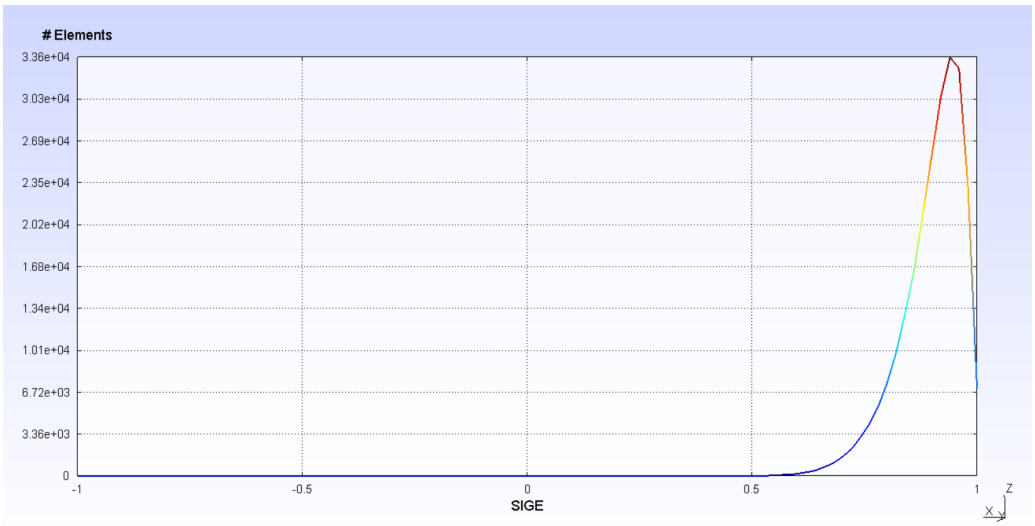

Source: Author.

3.2 CFD analysis: SU2

The goal of the analysis is to present a comprehensive understanding of the aerodynamic behavior of the wedge under hypersonic conditions. To achieve this, and given the complexity of the governing equations, the analysis will be conducted using Computational Fluid Dynamics. Simulations will be carried out with **SU2** (SU2 Developers, 2025), an advanced open-source software designed for the numerical solution of partial differential equations (PDE) and for performing PDE-constrained optimization. It uses finite element and finite volume methods to solve both steady and unsteady flow conditions, including turbulent and laminar flows. SU2 has been widely adopted in aerospace engineering and has proven effective in simulating complex geometries, offering tools for mesh generation, solution procedures, and post-processing, all in a flexible and efficient environment.

In CFD, the type of flow and the particular problem being examined determine which solver is used. In order to approximate the governing equations, these solvers vary in terms of the physical models they use and the numerical methods employed. For this study, an Euler solver will be used, which approximates the flow equations under the assumption that the flow is inviscid and compressible. The focus is on understanding the overall flow structure around the wedge and capturing key aerodynamic features without accounting for viscous effects, which are less significant in the regions of interest, which makes this choice of solver appropriate for the analysis being carried out.

Euler solvers are commonly used in high-speed aerodynamics where the effects of viscosity are minimal compared to the inertial and compressible forces. By using this solver, the analysis focuses on capturing the primary flow patterns, shock waves, and pressure distributions without the added complexity of viscous modeling.

3.2.1 Equations

These are the equations solved by the Euler method, based on the conservation equations for mass, momentum, and energy, which are essential for modeling the behavior of compressible fluid flows. Below are the key equations used in the formulation of fluid problems:

$$\frac{\partial \rho}{\partial t} + \frac{\partial (\rho u)}{\partial x} + \frac{\partial (\rho v)}{\partial y} + \frac{\partial (\rho w)}{\partial z} = 0$$

$$\rho \frac{\partial u}{\partial t} + \rho u \frac{\partial u}{\partial x} + \rho v \frac{\partial u}{\partial y} + \rho w \frac{\partial u}{\partial z} = -\frac{\partial p}{\partial x}$$

$$\rho \frac{\partial v}{\partial t} + \rho u \frac{\partial v}{\partial x} + \rho v \frac{\partial v}{\partial y} + \rho w \frac{\partial v}{\partial z} = -\frac{\partial p}{\partial y}$$

$$\rho\frac{\partial w}{\partial t} + \rho u\frac{\partial w}{\partial x} + \rho v\frac{\partial w}{\partial y} + \rho w\frac{\partial w}{\partial z} = -\frac{\partial p}{\partial z}$$

$$\frac{\partial s}{\partial t} + u\frac{\partial s}{\partial x} + v\frac{\partial s}{\partial y} + w\frac{\partial s}{\partial z} = 0$$

3.2.2 Freestream Properties and Flight Conditions

The selected altitude to perform the simulations is an altitude of h = 30 km, and according to the International Standard Atmosphere (ISA), the freestream properties will be set as seen in table 2.

The simulations will be conducted at three distinct Mach numbers and at four different angles of attack, following the dissertation (GUZMÁN-BOHÓRQUEZ, 2024).

	Symbol	**Value**	**Units**
Freestream Temperature	T_∞	231.83	K
Freestream Pressure	P_∞	1151.4	Pa
Mach number	M_∞	5,6,7	-
Angle of attack	AoA	-5,0,2,5	°

Table 2 – Freestream and flight conditions for the numerical simulations.

For the simulations, the freestream properties are modeled assuming an ideal gas, which is a common assumption in hypersonic and supersonic flow simulations. The temperature and pressure are determined using the ideal gas law: $p = \rho RT$.

Additionally, for the Euler solver used in this study, a value of $\gamma = 1.4$ is assumed, which is typical for air in compressible flow simulations. The value of γ represents the ratio of specific heats (c_p/c_v) and is crucial for modeling the compressible nature of the flow, as it influences the shock waves, temperature distribution, and overall aerodynamic behavior of the vehicle.

3.2.3 Simulations

The solver's setup is controlled through an input configuration file .cfg, which defines key parameters such as the CFL number, the implicit Euler time-stepping scheme, the selection of linear solvers, and the convergence criteria.

The relationship between the flow velocity, spatial resolution, and time step size is controlled by the **Courant-Friedrichs-Lewy number (CFL)**, which has been set to 0.3. In compressible flow simulations, the CFL number determines the stability and convergence of the solution. At this value, the simulation remains stable even for high-speed flows, where larger CFL numbers could potentially lead to instability while maintaining a manageable computational cost.

For this simulation, the **Implicit Euler** time-stepping scheme was chosen because of its stability, especially for stiff problems like hypersonic flows, which makes it popular in computational fluid dynamics (OOSTROM, 2015). The implicit method is unconditionally stable, allowing for larger time steps without compromising the accuracy of the solution. It has substantial benefits in terms of stability and efficiency when working with high-velocity flows, despite being computationally more costly because they require solving a system of equations at each time step.

In order to solve the system of equations that results from the discretization of the governing fluid flow equations, the **Flexible Generalized Minimal Residual (FGMRES)** solver has been chosen (PALACIOS F.; PADRON, 2014). FGMRES is an iterative method that works well for resolving implicit formulations, which are equations with a lot of unknowns. When combined with FGMRES, the preconditioner **Lower-Upper Symmetric Gauss-Seidel (LU_SGS)** improves the conditioning of the system, which increases the solver's convergence (ECONOMON, 2015).

The **residual** and **Cauchy convergence criteria** control the simulation's convergence. The residual value, which measures the difference between successive iterations of the solution, is tracked throughout the simulation. To ensure the accuracy of the results, a minimum residual value of -15 in logarithmic scale is set, meaning that the solution should be improved until the residual reaches this threshold.

The tolerance for the solution's convergence is determined by setting the epsilon value for the **Cauchy criteria** to 1E-6. This guarantees that when the solution stabilizes in the designated regions of interest and reaches a small enough residual error, the simulation will end. These criteria are essential for verifying that the lift and drag coefficients (C_L and C_D) and other aerodynamic quantities have stabilized and are trustworthy for further analysis.

4 RESULTS

Once the simulations are complete, the results will be visualized using **Paraview**, a powerful open-source tool for analyzing large-scale datasets. The study will begin with an examination of shock waves and Prandtl-Meyer expansions around the wedge, providing a fundamental understanding of the supersonic and hypersonic flow behavior.

The analysis will then focus on the effect of Mach number at a fixed angle of attack of 2°, studying its influence on the velocity profiles and pressure coefficient throughout the computational domain. Subsequently, the Mach number will be fixed at 6, and the angle of attack will be varied to investigate its impact on the flow structure and pressure distribution, highlighting changes in the shock wave patterns.

In addition to analyzing the flow field variables, the aerodynamic coefficients will be examined as well as their variations under each flight regime. This analysis will provide a quantitative assessment of the wedge's aerodynamic performance for different angles of attack and Mach numbers. Finally, in order to make sure that the calculated flow fields and aerodynamic coefficients are precise and representative of the physical phenomena, the convergence behavior of the simulations will be studied.

4.1 Shock waves and Expansions analysis

The hypersonic flow around the wedge rises complex aerodynamic phenomena, among which shock waves and expansions are particularly significant. Therefore, the analysis of these structures is necessary to determine variables such as the shape and position of the shock wave, and the pressure distribution on the vehicle surface. The analytical results will be compared with the ones obtained from the numerical simulations using SU2 in order to establish a reference framework.

The study case will be carried out with the results obtain in the simulation at M_∞ = 6 and AoA = 2°.

4.1.1 Oblique shock waves

In the intrados of the wedge, an oblique shock wave is formed. Unlike normal shock waves, which are perpendicular to the incoming flow, oblique shock waves are inclined with respect to the flow direction. This inclination produces less abrupt changes in the flow properties and allows a larger portion of the flow to remain in the supersonic regime after crossing the wave. Additionally, in the case of a waverider, the oblique shock waves are typically attached to the surface, forming a crucial component of the aerodynamic design. The attachment of these shock waves helps to maintain the desired lift-to-drag

ratio by minimizing flow separation and optimizing pressure distribution along the surface. This feature is key for maintaining stable, high-performance flight at hypersonic speeds.

The governing equations for these waves are similar to those of normal shock waves, but with a key difference: the calculations are not carried out directly with the incident Mach number, but instead with the component of the Mach number normal to the shock wave, both at the upstream and downstream sides of the flow. This normal component is obtained from the geometric relations between the flow direction and the inclination of the shock wave.

To determine the conditions of the incident flow (velocity, pressure, and temperature) and the downstream flow, two fundamental angles must be considered:

- β**:** Represents the angle formed between the oblique shock wave and the direction of the incoming flow. This angle is determined as a function of the Mach number and the flow deflection angle, δ.
- δ**:** Corresponds to the flow deflection angle, i.e., the angle formed between the direction of the flow after crossing the shock wave and the direction of the incident flow.

The mathematical relations between these angles, together with the conservation equations, allow the calculation of the flow properties downstream of the shock. The main resulting equations are the following:

$$\tan\delta = \frac{2}{\tan\beta}\cdot\left[\frac{M_1^2\sin^2\beta - 1}{2 + M_1^2\left(\gamma + \cos 2\beta\right)}\right] \tag{4.1}$$

$$M_1 = \frac{M_{1n}}{\sin\beta} \tag{4.2}$$

$$M_{2n}^2 = \frac{2 + (\gamma - 1)M_{1n}^2}{2\gamma M_{1n}^2 - (\gamma - 1)} \tag{4.3}$$

$$M_2 = \frac{M_{2n}}{\sin(\beta - \delta)} \tag{4.4}$$

$$\frac{p_2}{p_1} = 1 + \frac{2\gamma}{\gamma + 1}\left(M_1^2\sin^2\beta - 1\right) \tag{4.5}$$

$$\frac{\rho_2}{\rho_1} = \frac{(\gamma + 1)M_1^2\sin^2\beta}{(\gamma - 1)M_1^2\sin^2\beta + 2} \tag{4.6}$$

$$\frac{T_2}{T_1} = \frac{p_2/p_1}{\rho_2/\rho_1} = \left[1 + \frac{2\gamma}{\gamma+1} M_1^2 \sin^2\beta\right] \cdot \left[\frac{(\gamma-1)M_1^2 \sin^2\beta + 2}{(\gamma+1)M_1^2 \sin^2\beta}\right] \tag{4.7}$$

The angle β is estimated with the aid of Paraview's built-in tool for angle measurement and the streamline viewer, resulting in an angle of approximately $\beta = 16°$ for the selected incident Mach number. By applying the aforementioned equations (with $\gamma = 1.4$ for air) and using the oblique shock tables, the results summarized in Table 3 are obtained.

Variable	**Value**
δ	8.30°
M_2	4.57
p_2	3482.21 Pa
T_2	457.96 K

Table 3 – Flow conditions downstream of the oblique shock wave.

4.1.2 Prandtl–Meyer Expansion

Another phenomenon of interest in the study of bodies in hypersonic flow is the Prandtl–Meyer expansion fan, where the expansion of a uniform hypersonic stream sliding along a convex corner takes place. These expansion phenomena occur in regions where the flow moves toward areas of lower pressure, typically around the trailing edges of the vehicle or in zones where the body geometry changes abruptly. Such expansions help reduce the local pressure, but they also influence the aerodynamic stability and the forces acting on the vehicle.

In the present configuration, this phenomenon occurs on the upper surface at the leading edge as a consequence of the positive angle of attack. It is important to note that if the angle of attack were zero, no expansion would be generated at this location. This process is governed by the Prandtl–Meyer expansion waves, which form a continuous set of characteristic waves that enable the flow to accelerate and expand while following the new direction. Additionally, expansions also develop at the trailing edges of the wedge, since the geometry ends with a 90° angle that forces the flow to diverge, that is, it departs from the original flow direction, causing the fluid particles to expand along a trajectory that adapts to the new contour.

The expressions that allow determining the deflection angles and the downstream Mach number are as follows:

$$\theta = \sqrt{\frac{\gamma+1}{\gamma-1}} \arctan\left[\sqrt{\frac{\gamma-1}{\gamma+1}}\,(M^2-1)\right] \tag{4.8}$$

$$\alpha = \arcsin\left(\frac{1}{M}\right) = \arctan\left(\frac{1}{\sqrt{M^2-1}}\right) \tag{4.9}$$

$$\frac{p}{p_0} = \left(\frac{2}{2+(\gamma-1)M^2}\right)^{\frac{\gamma}{\gamma-1}} \tag{4.10}$$

$$\frac{p_2}{p_1} = \left(\frac{2+(\gamma-1)M_1^2}{2+(\gamma-1)M_2^2}\right)^{\frac{\gamma}{\gamma-1}} \tag{4.11}$$

According to the wedge geometry, an estimated deflection angle of 2° is obtained. For this value, the incoming Mach number parallel to the wall, at which the expansion begins, is $M = 6$. By performing the calculations with the previously introduced equations and with the aid of the Prandtl–Meyer expansion tables, the results summarized in Table 4 are obtained.

Variable	**Value**
M_2	6.30
p_2	849.09 Pa

Table 4 – Flow conditions downstream of the Prandtl–Meyer expansion.

4.1.3 SU2 results

Figure 26 – Mach distribution

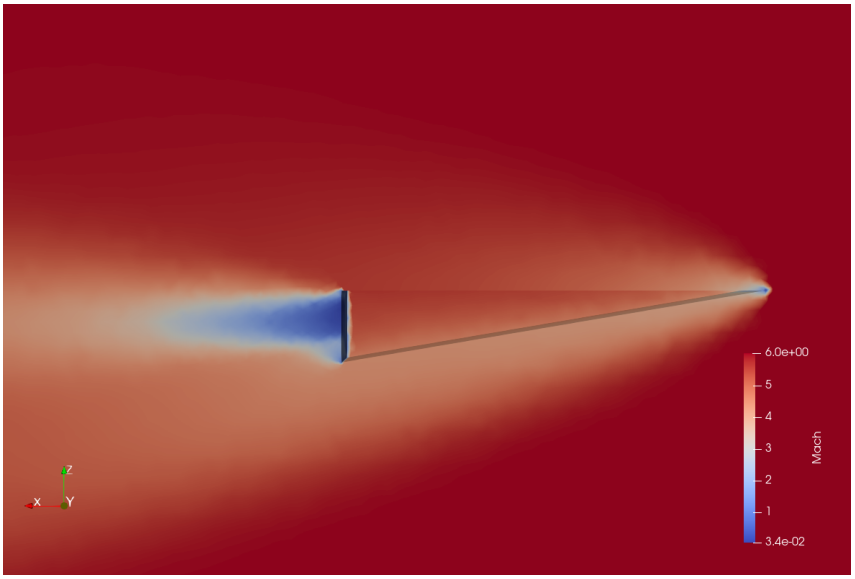

Source: Author.

On the SU2 simulation the Mach number after the oblique shock wave is approximately 4.308, compared to 4.57 obtained using the expression for an oblique shock evaluated earlier. On the other hand, the Prandtl-Meyer expansion has not been accurately captured by the simulation. The results are obscured by the shock stagnation point, obtaining unrealistic values.

Furthermore, it must be considered that the calculations are performed for a 2D shock wave, while the simulation models a 3D flow. The 2D model being used assumes a simplified geometric shape and does not account for the three-dimensional effects that may be present in the simulation. In the 3D simulation, the shock wave behavior can be more complex, exhibiting curvature or deflection due to the influence of the object's geometry and the flow shape. The 2D model is limited to describing planar shock waves, which may lead to discrepancies with the actual 3D simulation.

Figure 27 – Pressure coefficient distribution

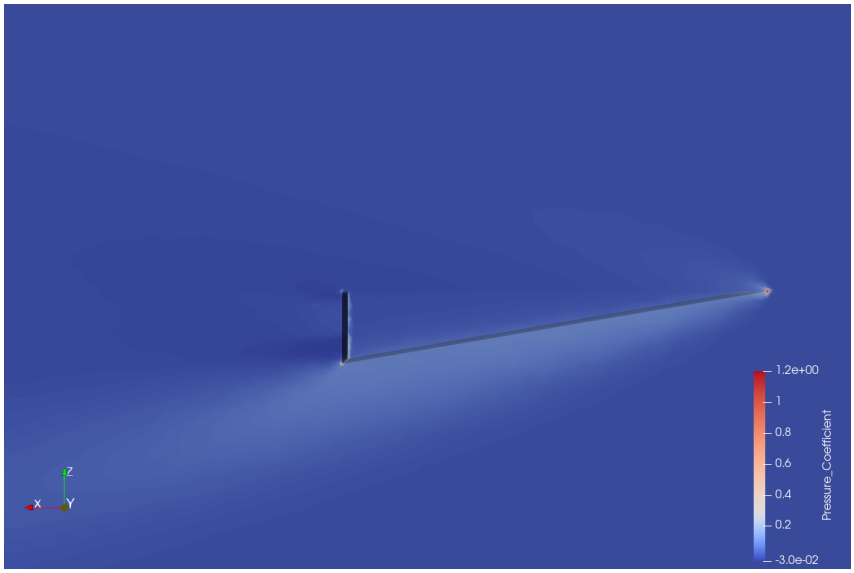

Source: Author.

As expected, a significant increase in the pressure coefficient is observed in the region near the stagnation point of the capsule. The pressure value reached after the shock wave is 3482.21 Pa, compared to 3500.48 Pa obtained through the previous algebraic expressions. For pressure, the analytical and numerical models are much closer in comparison.

Figure 28 – Temperature distribution

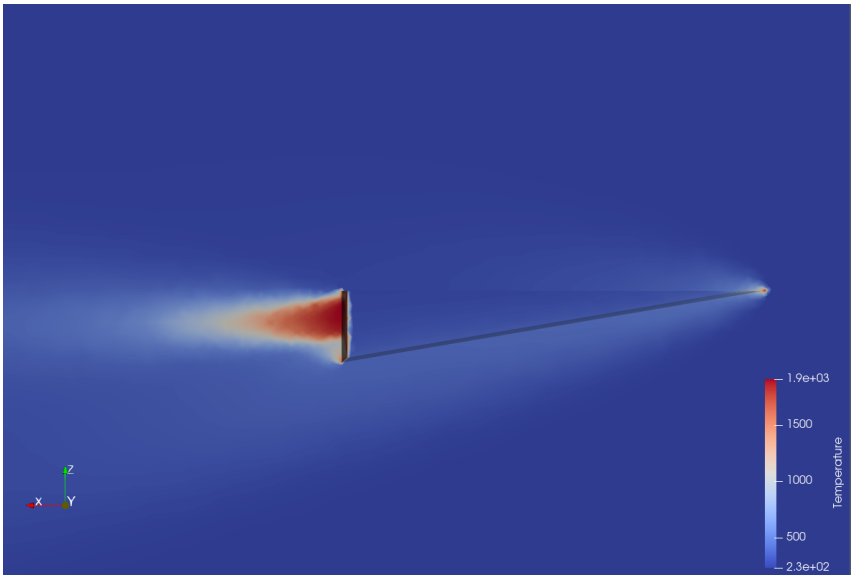

Source: Author.

Before analyzing the temperature, it is important to note that, in the absence of viscosity, the temperature increase is solely attributed to phenomena related to the intense compressions generated by the shock waves.

Regarding the temperature of the flow immediately after the shock wave, it is 420.334 K, compared to the 457.96 K calculated previously.

4.2 Shock wave variation with Mach number

4.2.1 Mach distribution at constant AoA:2°

Figure 29 – Mach distribution for $M_\infty = 5$

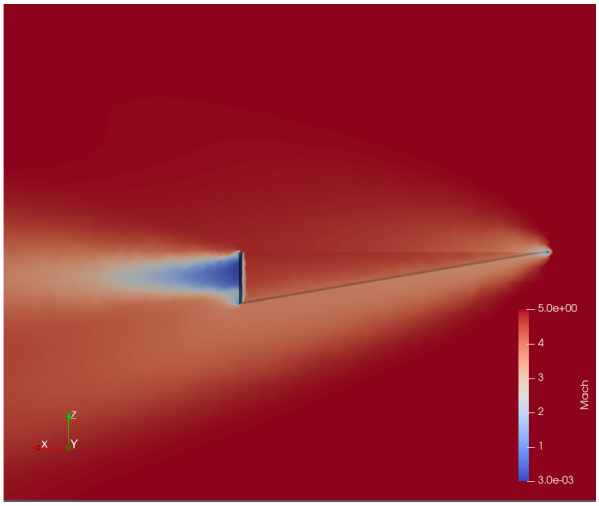

Source: Author.

Figure 30 – Mach distribution for $M_\infty = 6$

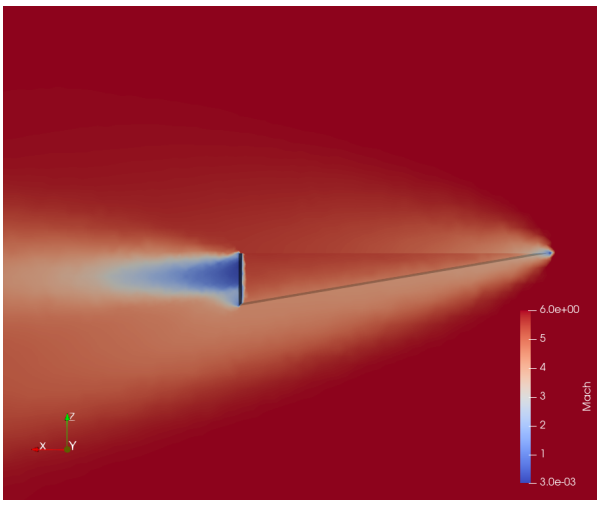

Source: Author.

Figure 31 – Mach distribution for $M_\infty = 7$

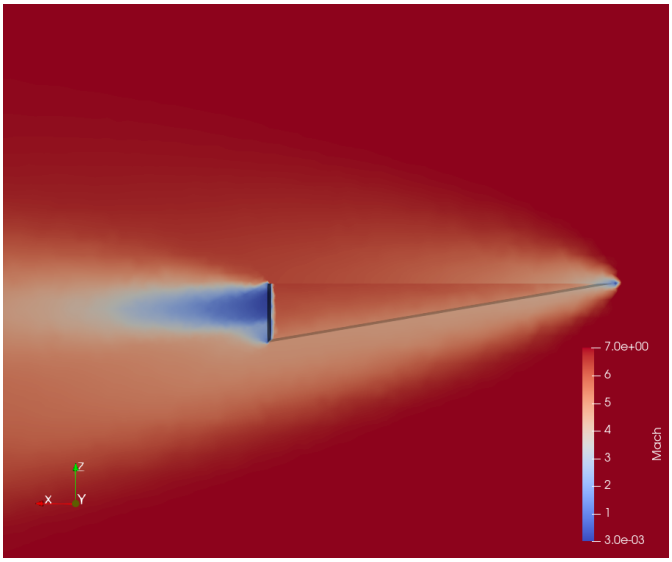

Source: Author.

The analysis of the Mach number distribution around the wedge at a fixed angle of attack of 2° shows consistent trends with classical compressible flow theory. In all three cases studied an attached oblique shock is generated at the lower surface of the wedge, while the upper surface is subjected to a weak expansion. At the leading edge, the velocity is observed to drop to zero, identifying the expected stagnation point, which confirms the accuracy of the numerical results and the fidelity of the boundary conditions applied in the simulation.

As the freestream Mach number increases, the shock attached to the intrados becomes progressively leaner. From theoretical considerations of oblique-shock relations, it is known that the shock angle decreases with increasing Mach number; however, in the present visualizations this reduction is not appreciable, as the shock inclination remains nearly unchanged across the cases.

Another consistent observation is that the flow downstream of the shock remains supersonic in all cases, which is in agreement with the weak-shock solution expected for such a small deflection angle. This confirms that the compression generated by the wedge is sufficient to produce lift through shock attachment without causing a normal shock in front of the body.

Near the trailing edge the flow undergoes a recompression due to the abrupt geometry change. As a result, the velocity field shows a local reduction downstream of the trailing edge, consistent with the closing of the expansion fan and the adjustment of the flow to the wake.

4.2.2 Pressure coefficient distribution at constant AoA: 2°

Figure 32 – C_p distribution for $M_\infty = 5$

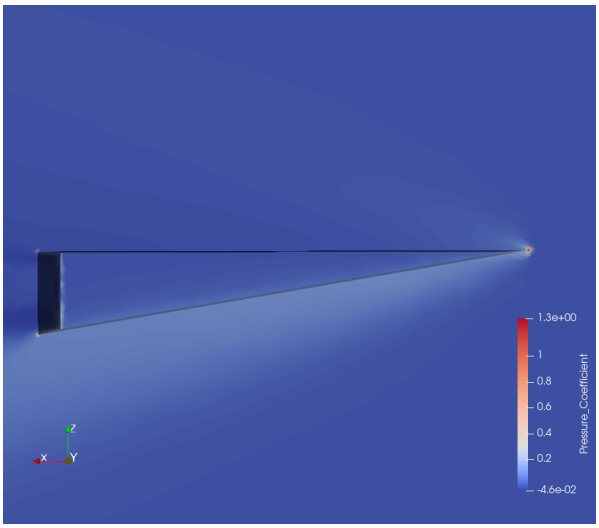

Source: Author.

Figure 33 – C_p distribution for $M_\infty = 6$

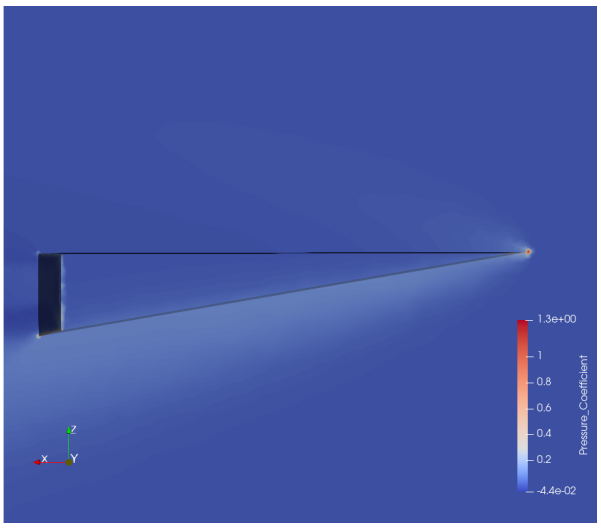

Source: Author.

Figure 34 – C_p distribution for $M_\infty = 7$

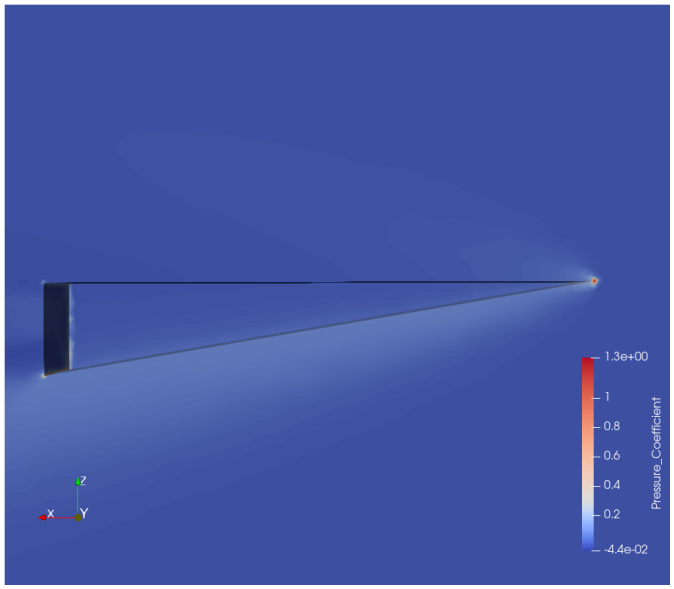

Source: Author.

The pressure coefficient distributions along the wedge surfaces at a fixed angle of attack of 2° show consistent features across the three freestream Mach numbers considered. On the lower surface, where the attached shock is formed, the coefficient of pressure reaches its maximum values very close to the leading edge. This concentration of pressure near the front of the wedge is clearly visible in all cases and reflects the immediate compression generated by the incident shock.

As the Mach number increases, the spatial extent of this high-pressure region becomes progressively narrower. Further downstream along the lower surface, the coefficient of pressure decreases smoothly toward more moderate values. The slope of this decay becomes slightly steeper at higher Mach numbers, which visually corresponds to the thinner post-shock layer observed in the Mach contour plots.

At the trailing edge, both surfaces show the influence of the wake development. In this region, the coefficient of pressure can take slightly negative values, particularly evident near the lower surface where the flow adjusts into the wake. This local effect highlights the loss of pressure recovery at the sharp trailing edge and the presence of a low-pressure core associated with wake formation, which is consistently visible across all Mach numbers.

4.3 Shock wave variation with Angle of attack

4.3.1 Mach distribution at constant M_∞: 6

Figure 35 – Mach distribution for AoA=−5°

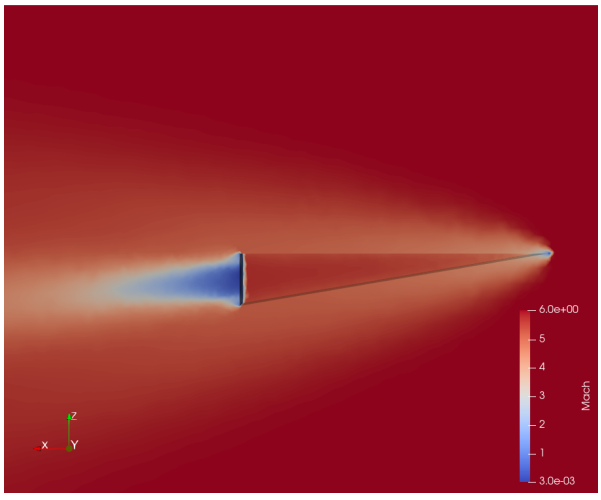

Source: Author.

Figure 36 – Mach distribution for AoA=0°

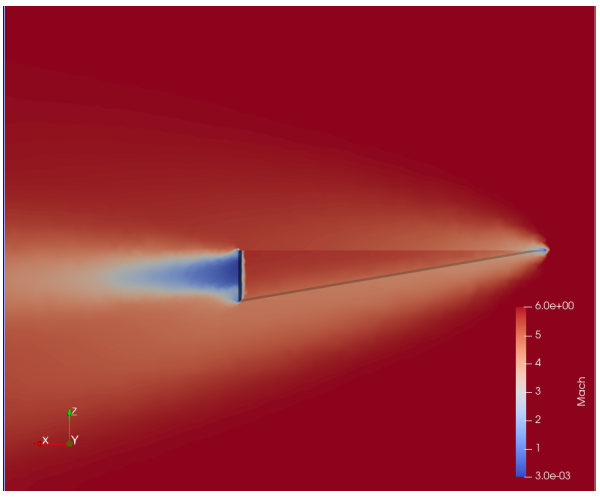

Source: Author.

Figure 37 – Mach distribution for AoA=2°

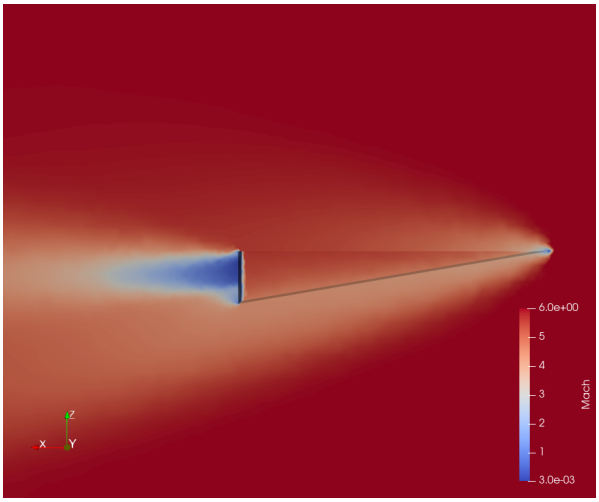

Source: Author.

Figure 38 – Mach distribution for AoA=5°

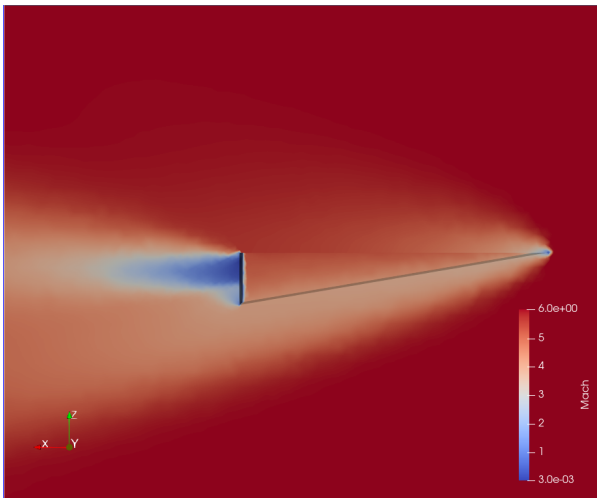

Source: Author.

The Mach number distributions at fixed freestream Mach 6 reveal that the angle of attack primarily governs the redistribution of compression and expansion around the wedge. As the incidence shifts from negative to positive values, the dominant compression region, characterized by a visible low-Mach pocket downstream of the attached shock, migrates from the upper surface to the lower surface, while the extrados develops an increasingly extended Prandtl–Meyer expansion with locally higher Mach numbers.

The strength and area of the shock layer grow with the magnitude of the incidence, placing the compressed flow closer to the surface on the side facing the oncoming flow deflection. Across all cases, the post-shock flow remains supersonic, and the stagnation point at the leading edge is consistently identifiable by the local velocity drop. Finally, the wake downstream of the trailing edge shows a persistent Mach-deficit core, which becomes broader and more asymmetric as the angle of attack increases in magnitude, reflecting the upstream imbalance between compression and expansion.

4.3.2 Pressure coefficient distribution at constant M_∞: 6

Figure 39 – C_p distribution for AoA=−5°

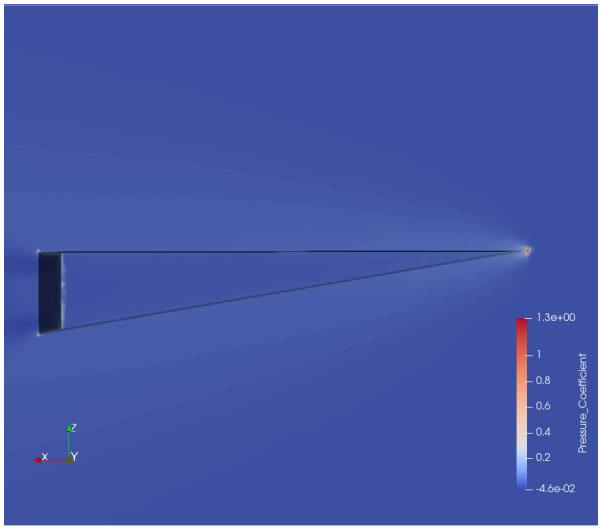

Source: Author.

Figure 40 – C_p distribution for AoA=0°

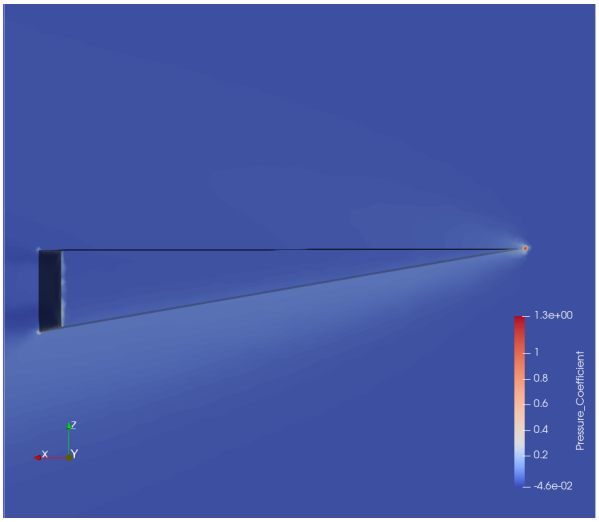

Source: Author.

Figure 41 – C_p distribution for AoA=2°

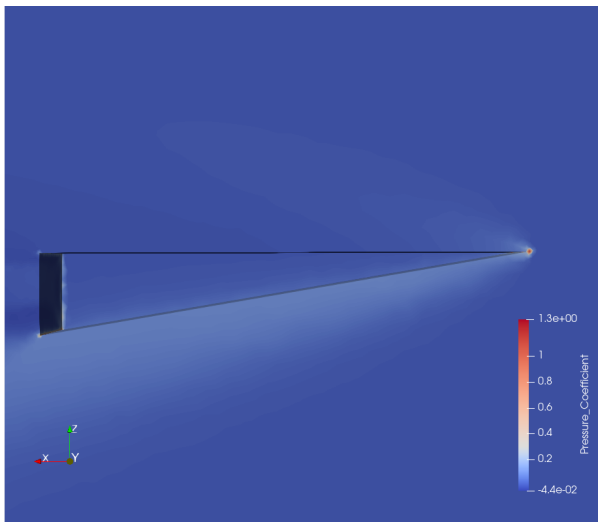

Source: Author.

Figure 42 – C_p distribution for AoA=5°

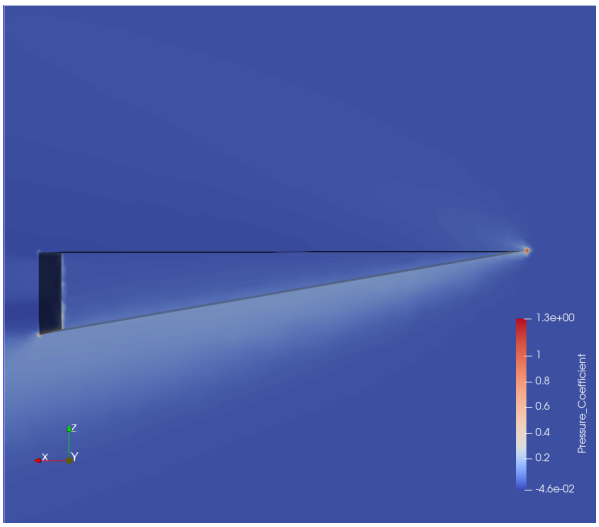

Source: Author.

The pressure coefficient distributions at Mach 6 clearly reflect how the aerodynamic loading shifts with angle of attack. For negative incidence, the peak positive pressure is concentrated at the leading edge of the upper surface, while the lower surface exhibits predominantly negative values indicative of expansion. At zero incidence, the lower surface displays a strong pressure peak close to the leading edge, whereas the upper surface remains nearly neutral, producing a visibly asymmetric distribution consistent with the wedge geometry.

As the angle of attack increases to 2° and then to 5°, the maximum Cp on the intrados becomes sharper and more confined to the leading edge, while the extrados develops increasingly negative values that extend toward the trailing edge.

In all cases, the wake region at the rear is associated with a localized negative Cp signature, reflecting the low-pressure core formed downstream. Overall, the images demonstrate that raising the incidence progressively intensifies the compression on the lower surface and enhances the suction on the upper surface, with both effects becoming more pronounced and spatially localized as the angle of attack grows.

4.4 Aerodynamic Coefficients

This section will focus on the analysis of the aerodynamic coefficients, namely the lift coefficient (C_L), drag coefficient (C_D), and lift-to-drag ratio (L/D), and how they are influenced by the Mach number and angle of attack. These findings also come from simulations that were run with SU2. Optimizing the aerodynamic performance of high-speed vehicles requires an understanding of how these coefficients change with variations in Mach and angle of attack. This analysis is especially pertinent to the study since it provides a thorough assessment of the geometry's flow properties and efficiency, both of which are critical for upcoming developments in aerospace vehicle design.

Mach	AoA	C_L	C_D	L/D
5	$-5°$	-0.002852	0.005109	-0.5582
	0°	0.069799	0.012198	5.7222
	2°	0.100467	0.019631	5.1178
	5°	0.149542	0.036352	4.1137
6	$-5°$	-0.002839	0.001876	-1.5133
	0°	0.058223	0.007884	7.3850
	2°	0.084754	0.014304	5.9252
	5°	0.128523	0.029058	4.4230
7	$-5°$	-0.002783	-0.000143	19.4615
	0°	0.050122	0.005104	9.8201
	2°	0.073771	0.010808	6.8256
	5°	0.113856	0.024170	4.7106

Table 5 – Aerodynamic Coefficients and Lift-to-Drag ratio for each simulation

Figure 43 – Lift Coefficient vs. AoA

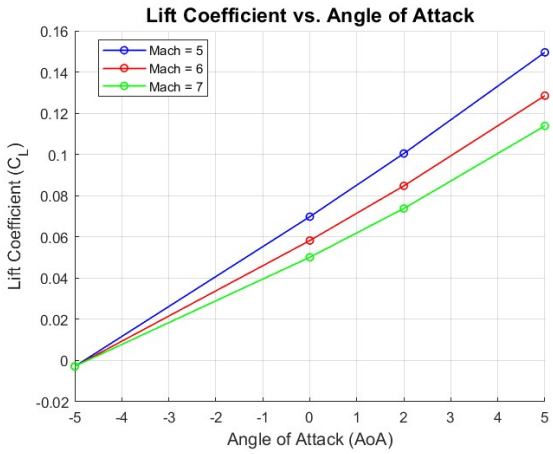

Source: Author.

Figure 44 – Lift Coefficient vs. Mach

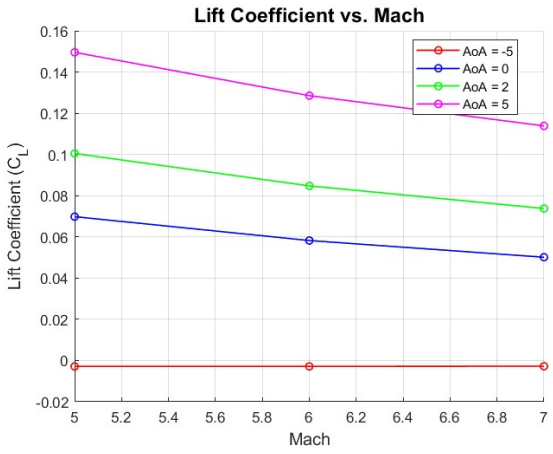

Source: Author.

The lift coefficient varies almost linearly with the angle of attack, with higher angles producing proportionally larger lift. This linearity confirms the expected aerodynamic behavior of slender bodies at hypersonic speeds and illustrates that angle of attack a key driver of lift generation.

The lift coefficient shows only a weak dependence on the Mach number across the hypersonic range, remaining essentially dictated by the angle of attack. This near constancy is a direct manifestation of the hypersonic Mach independence, whereby aerodynamic coefficients become nearly invariant with respect to Mach number at very high speeds.

Figure 45 – Drag Coefficient vs. AoA

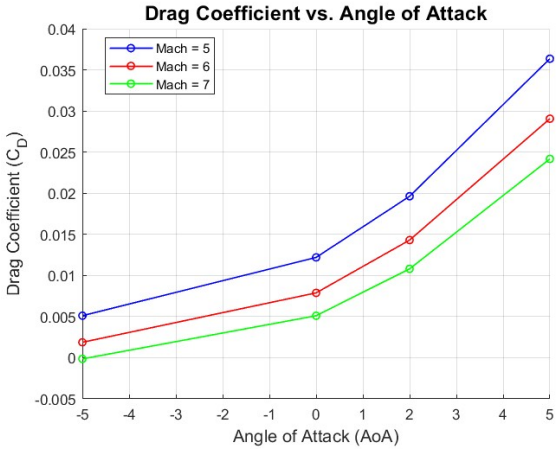

Source: Author.

Figure 46 – Drag Coefficient vs. Mach

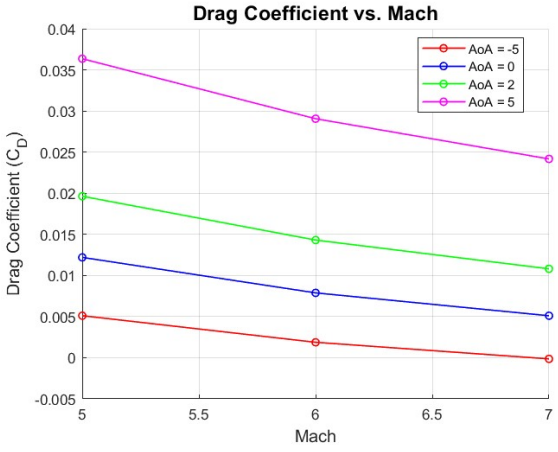

Source: Author.

The drag coefficient follows a parabolic trend with respect to angle of attack, reaching a minimum near zero incidence and increasing symmetrically for larger positive or negative angles. This behavior reflects the quadratic dependence of induced and pressure drag on the deflection from the free-stream direction.

The drag coefficient exhibits a slight reduction as Mach number increases, but its overall variation remains minor. This weak sensitivity again reflects the Mach independence characteristic of hypersonic flows, with the dominant effect being the geometric configuration and angle of attack rather than Mach number itself.

Figure 47 – Lift-to-Drag Ratio vs. AoA

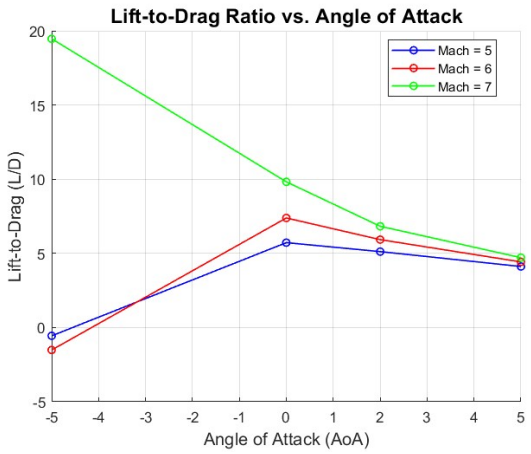

Source: Author.

Figure 48 – Lift-to-Drag Ratio vs. Mach

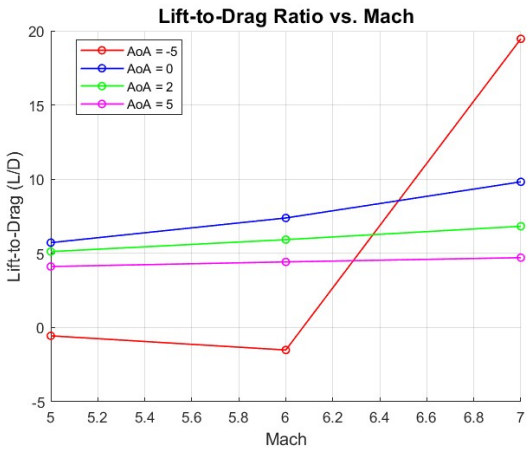

Source: Author.

Up to about 0°, the lift-to-drag ratio rises with the angle of attack to its maximum value before stabilizing. This is due to the fact that any lift above this threshold is counterbalanced by a notable increase in drag, which results in a plateau in L/D. Particularly in the hypersonic regime, L/D typically exhibits an increasing trend as Mach rises. The flow becomes more streamlined at higher Mach numbers, which lessens the effect of drag and increases aerodynamic efficiency. However, the particular configuration and flow conditions limit the increase in L/D.

The exceptionally small and even negative drag coefficient observed at AoA = -5° and Mach = 7 is responsible for the observed anomaly, where the lift-to-drag ratio reaches abnormally high values. The drag coefficient in hypersonic flows, particularly at high Mach numbers, is extremely sensitive to small variations in pressure distribution, shear forces, and the intricate relationships between the boundary layers and shock waves. This anomaly could be the result of the near-zero value of drag, causing the L/D ratio to become artificially large. The appearance of negative drag, which does not correspond to any physically realistic aerodynamic situation, indicates the presence of numerical artifacts rather than a genuine physical phenomenon. The absence of viscosity effects in the current model could contribute to this unrealistic behavior, as viscous forces, which are often significant in real-world hypersonic flows, are not considered in this Euler inviscid flow model. Additionally, breaking down the drag coefficient into its components: pressure drag ($C_{D,p}$) and friction drag ($C_{D,f}$), can help identify which specific contribution is leading to the problem. The negative value of C_D suggests a miscalculation or imbalance in the pressure forces, which may be incorrectly represented in the numerical scheme.

Furthermore, it is possible that the computational domain, or control volume, is not sufficiently large to capture the relevant flow features, leading to a poor representation of the physics and further contributing to the observed anomaly.

Figure 49 – Drag Polar Curve

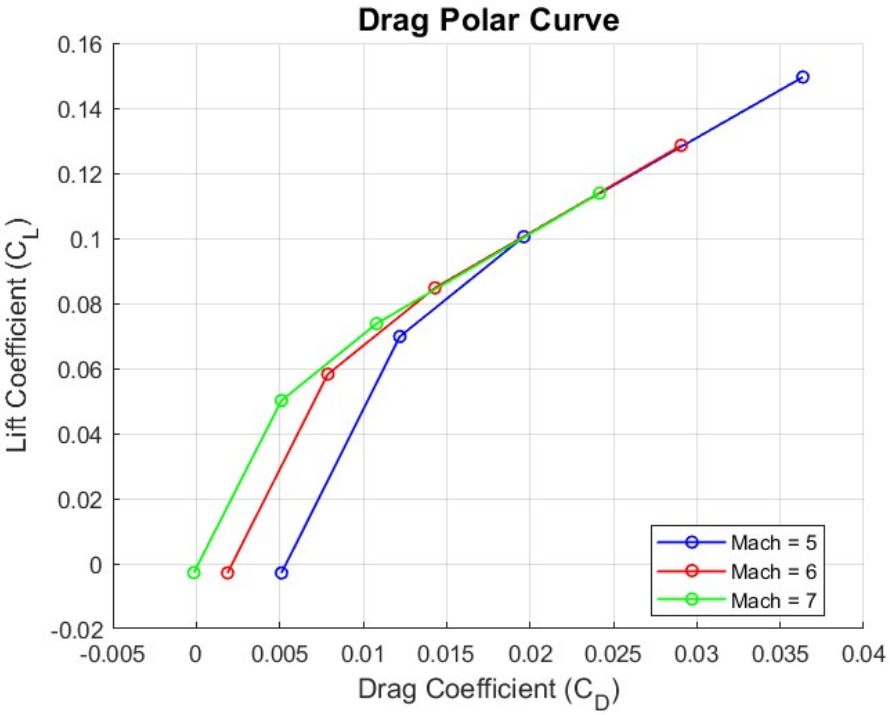

Source: Author.

The polar curve shows a typical parabolic shape, where drag increases as the square of lift, consistent with classical aerodynamic theory. This relationship reflects the fundamental trade-off between lift and drag: as lift increases, drag also increases, but at a faster rate. The "efficiency envelope," or the range where the lift-to-drag ratio (L/D) is maximized, is highlighted in the curve that depicts the configuration's aerodynamic efficiency. At moderate lift coefficients, the configuration operates near its optimal point, where the lift is sufficiently high while drag remains relatively low. The curve also indicates regions where the design may become less efficient, showing a fast performance deterioration as drag overcomes lift at high angles of attack or lift coefficients.

Figure 50 – Lift-to-Drag Ratio vs. Lift Coefficient

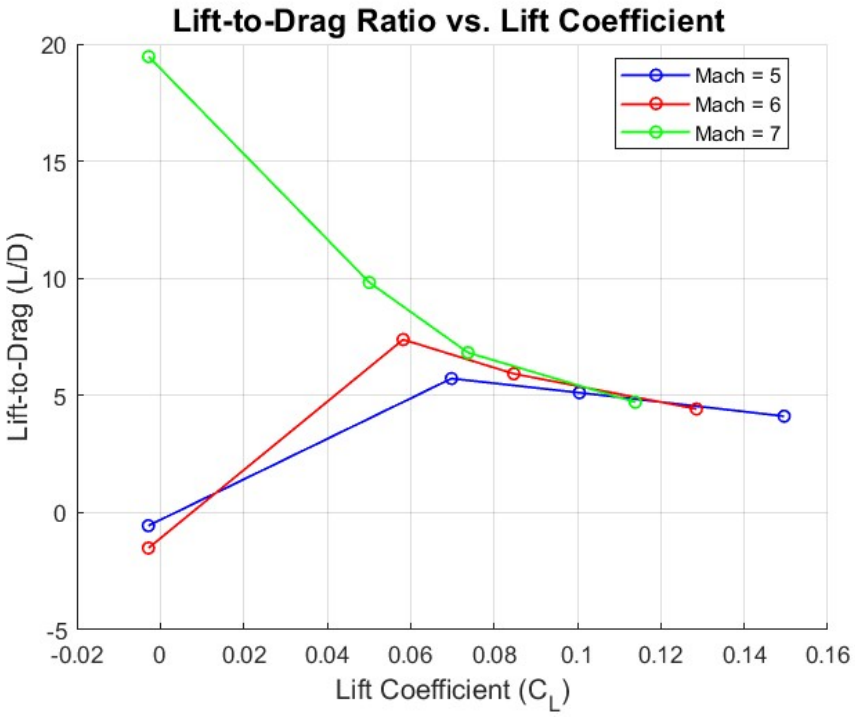

Source: Author.

The lift-to-drag ratio reaches its maximum at intermediate lift coefficients, corresponding to AoA = 0°, where the balance between lift generation and drag penalty is most favorable. At very low or very high lift values, the efficiency decreases due to either negligible lift or rapidly growing drag. The results highlight the trade-off between generating lift and maintaining aerodynamic efficiency, which is crucial for optimizing hypersonic vehicle designs.

4.5 Convergence behavior

The residuals in the **history output file** prints out the convergence behavior of the simulation. The values are given in a log10 format, meaning the negative values correspond to the exponent of 10 for the actual magnitude of the residual. Convergence is typically deemed satisfactory when the residuals fall to around $10^{-}6$ or lower, indicating that the solution is sufficiently close to the true physical solution. Throughout the simulation, the residuals for different angles of attack and Mach numbers exhibit small variations but with a consistently decreasing tendency, indicating that the solution is converging well and that the solver is accurately modeling the flow field. The residuals being tracked are:

- **rms**[**Rho**]: residual of mass conservation (continuity equation).
- **rms**[**RhoU**]: residual of the momentum equation in the X direction.

- **rms**[**RhoV**]: residual of the momentum equation in the Y direction.
- **rms**[**RhoW**]: residual of the momentum equation in the Z direction.
- **rms**[**RhoE**]: residual of total energy conservation.

Mach	**AoA**	**rms**[**Rho**]	**rms**[**RhoU**]	**rms**[**RhoV**]	**rms**[**RhoW**]	**rms**[**RhoE**]
5	$-5°$	-15.05595113	-11.94522694	-12.52069455	-12.48448048	-8.976016265
	0°	-15.00202404	-11.92202924	-12.42744324	-12.42098815	-8.936582471
	2°	-15.00025196	-11.92483992	-12.42866978	-12.42457148	-8.939055834
	5°	-15.00151506	-11.90604407	-12.41366844	-12.41054166	-8.921195359
6	$-5°$	-15.0024207	-11.86359459	-12.41144157	-12.37465616	-8.828968684
	0°	-15.000268	-11.83032598	-12.34487853	-12.32859888	-8.788705043
	2°	-15.00249951	-11.83592698	-12.35037377	-12.3349828	-8.792942386
	5°	-15.00015891	-11.82320005	-12.34110406	-12.32722736	-8.779146789
7	$-5°$	-15.02743556	-11.80090696	-12.32626998	-12.2842756	-8.692919659
	0°	-15.00218649	-11.76366885	-12.28660099	-12.26146696	-8.66841055
	2°	-15.00173467	-11.77324456	-12.29239706	-12.26711317	-8.675946269
	5°	-15.00239476	-11.76014707	-12.28525846	-12.26203429	-8.66039365

Table 6 – Residuals for each simulation

For Mach 5, the most negative residuals in the momentum equations in the X, Y, and Z directions, as well as in total energy conservation are achieved when compared with the other Mach simulations. Higher Mach numbers tend to result in sharper gradients and stronger discontinuities in the flow field, that is why the solver may converge faster and more accurately for momentum and energy equations at Mach 5 due to the inherent nature of these flows at high speeds.

The residual for mass conservation is close to machine precision (10^{-16}) for all simulated cases. This is expected because mass conservation is a fundamental principle, and in well-behaved flows, it tends to be satisfied to a very high degree of accuracy.

The angle of attack influences the residuals significantly, with the best convergence at AoA $-5°$. At this angle of attack, the flow may be experiencing a more stable shock structure or less turbulent boundary layers which translates into a better convergence, as the solver would not have to resolve large-scale oscillations or instabilities, allowing it to reach more precise values in fewer iterations.

Figure 51 – Residual convergence Mach = 5, AoA = 0°

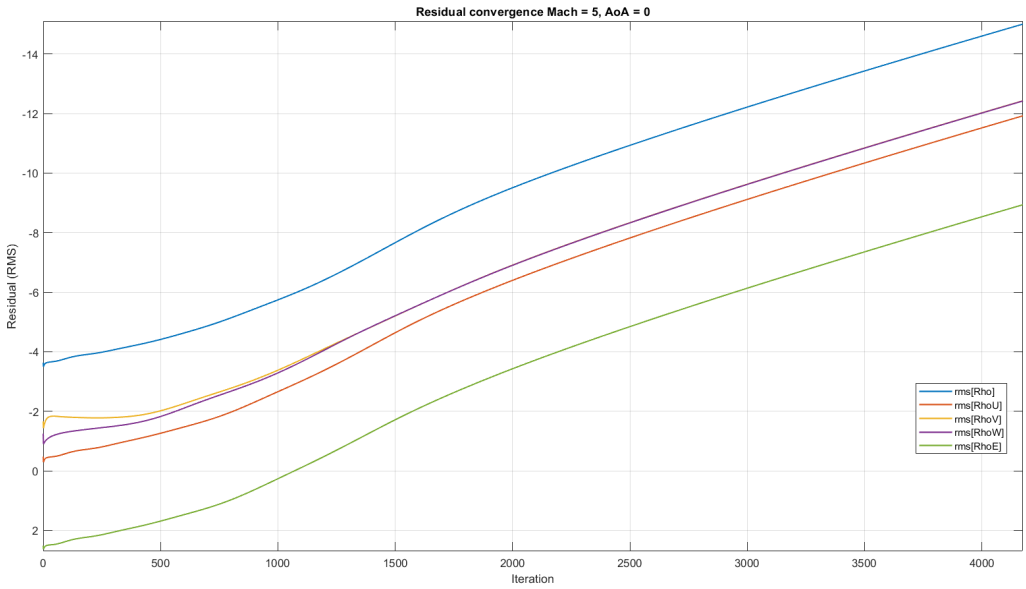

Source: Author.

In Figure 4.5, the logarithmic convergence of each residual for the simulation at Mach = 5 and AoA = 0 is shown. All residuals exhibit a decreasing trend, becoming more negative with each iteration. It can be observed that rms[Rho] is the one that reaches the convergence criterion.

5 CONCLUSION

The comparison between the SU2 simulation and the analytical results shows some discrepancies, particularly in the Mach number after the oblique shock and the Prandtl-Meyer expansion. The simulation, while generally close to the expected results, does not capture the expansion accurately due to the influence of the shock stagnation point. Additionally, the 2D analytical model simplifies the geometry, overlooking the more complex 3D effects observed in the simulation, such as shock wave curvature and deflection. Despite these differences, the pressure results from both approaches are in good agreement. The temperature increase observed in the simulation is attributed to compressional heating, consistent with the shock wave effects. To enhance the accuracy of the simulation, it would be beneficial to refine the mesh near the leading edge, allowing for better resolution of the shock and flow interactions.

The findings show that raising the freestream Mach number while maintaining a fixed angle of attack of 2° maintains the attached shock's overall structure and the post-shock flow's supersonic nature with little change in the shock angle. These results show the reliability of the computational results and the theoretical predictions. The maximum pressure is concentrated close to the leading edge of the intrados, and the pressure coefficient distribution is affected by the spatial redistribution of aerodynamic loading as the Mach number rises. The flow patterns seen in the Mach number fields are consistent with the upper surface's weak contribution to the pressure distribution.

At Mach 6, varying the angle of attack predominantly redistributes the location and intensity of the shock-induced compression and expansion, with the shock moving between the upper and lower surfaces based on the angle of attack. The pressure coefficient distributions show this, with the leading-edge peak shifting and becoming more intense as positive incidence rises. According to the analysis, even minor changes in geometry have a big impact on the flow topology because positive incidence increases suction over the upper surface and intensifies compression on the lower surface, while negative incidence moves the shock to the upper surface. These findings emphasize the significance of geometric optimization in hypersonic wedge configurations by demonstrating how sensitive shock structure and aerodynamic loading are to angle of attack.

The analysis of the shock wave, pressure coefficient, and Mach number distributions across various angles of attack and freestream Mach numbers demonstrates the complex interplay between flow characteristics and aerodynamic performance. As the angle of attack increases, the shock structure shifts and intensifies, primarily affecting the lower surface compression and upper surface expansion. The Mach fields reveal how compression regions grow and become more localized with higher incidence, while the pressure coefficient

distributions confirm the enhanced lift generation and increased suction at higher angles. The lift-to-drag ratio shows a moderate improvement with increasing lift, though it is limited by the concurrent rise in drag. Overall, the results emphasize the sensitivity of aerodynamic behavior to both Mach number and angle of attack, underscoring the importance of geometry optimization in hypersonic vehicle design.

Regarding the drag coefficient at an angle of attack of -5°, it is recommended to reassess the model's assumptions, specifically those concerning the neglect of viscosity. It is crucial to carefully evaluate the interactions between the shock waves, pressure distribution, and boundary layer effects to ensure that more accurate and physically consistent results are obtained. This reassessment will help refine the model and improve the prediction of aerodynamic performance at extreme conditions. Additionally, the issue might be alleviated by enlarging the control volume, which could reduce numerical errors and improve the stability of the solution.

As for the DFC, convergence of all the governing equations has been achieved with minimal residuals, demonstrating that the numerical results are both stable and reliable. The solver has successfully minimized errors in momentum, energy, and mass conservation, with the mass conservation residuals reaching near machine precision (10^{-16}). This high level of convergence reflects the accuracy of the results, providing a strong foundation for future work.

Building on this solid base, the next step would involve scaling the current model to a more computationally intensive simulation, incorporating a solver that accounts for viscosity and such as **Navier-Stokes**. Additionally, using a real gas model in SU2 would enhance the fidelity of the analysis, allowing for more detailed insights into the flow behavior under realistic.

REFERENCES

Geuzaine, C.; Remacle, J. Gmsh reference manual. 2025. Available at: <https://gmsh.info/dev/doc/texinfo/gmsh.pdf>.

ANDERSON, J. **Fundamentals of Aerodynamics**. [*S.l.: s.n.*]: McGraw-Hill Education, 1984. 314 p.

BAUER S.X.S.; COVELL, P. F. D. M. B. Preliminary assessment of a mach 4 and a mach 6 waverider. **1st International Hypersonic Waverider Symposium**, 1990. Available at: https://www.researchgate.net/publication/264751397_Preliminary_Assessment_of_a_Mach_4_and_a_Mach_6_Waverider.

BIN X.; ZHONGKE, S. An overview on flight dynamics and control approaches for hypersonic vehicle. **Science China Information Sciences**, 2015. Available at: https://www.researchgate.net/publication/276855141.

BOEING. X-51a waverider backgrounder. **The Boeing Company**, 2005. Available at: http://www.boeing.com/assets/pdf/defense-space/military/waverider/docs/X-51A_overview.pdf.

CORDA, S. Viscous optimized hypersonic waveriders designed from flows over cones and minimum drag bodies. **UMI**, 1988. Available at: https://www.proquest.com/docview/303584934?pq-origsite=gscholar&fromopenview=true&sourcetype=Dissertations%20&%20Theses.

DING F.; LIU, J. S. C. L. Z. C. S. F. X. An overview of research on waverider design methodology. **Acta Astronautica 140**, 2017. Available at: https://www.sciencedirect.com/journal/acta-astronautica.

ECONOMON, T. Su2: An open-source suite for multiphysics simulation and design. **American Institute of Aeronautics and Astronautics**, 2015. Available at: https://arc.aiaa.org/doi/abs/10.2514/1.j053813.

EGGERS A.J.; ASHLEY, H. S. G. Hypersonic waverider configurations from the 1950's to the 1990 's. **1st International Hypersonic Waverider Symposium**, 1990. Available at: https://ntrs.nasa.gov/citations/19910041106.

GATLAND, K. Commonwealth astronautics. **The Aeroplane and Astronautics**, 1959.

GONOR A.L.; KAZAKIV, M. S. A. S. V. Aerodynamic characteristics of star-shaped bodies at supersonic velocities. **Kluwer Academic Publishers-Plenum Publishers**, 1971. Available at: https://www.scopus.com/pages/publications/34250431380.

GUZMÁN-BOHÓRQUEZ, R. **Aerodynamic Analysis Applied to Hypersonic Waveriders through CFD**. 2024. 100 p. Dissertação (Engenharia Mecânica (Aeronáutica)) — Escola de Engenharia de São Carlos, Universidade de São Paulo, São Carlos, 2024.

HE X.; LE, J. W. Y. Design of a curved cone derived waverider forebody. **American Institute of Aeronautics and Astronautics**, 2009. Available at: https://arc.aiaa.org/doi/abs/10.2514/6.2009-7423.

HUANG W.; MA, L. W. Z. P. M. I. D. L. S. L. J. A parametric study on the aerodynamic characteristics of a hypersonic waverider vehicle. **Acta Astronautia 69**, 2011. Available at: https://www.sciencedirect.com/science/article/pii/S0094576511000555.

JERKINS, D. X-15 extending the frontiers of flight. **National Aeronautics and Space Administration**, 2012. Available at: https://www.nasa.gov/history/x-15-extending-the-frontiers-of-flight/.

JONES J.G.; MOORE, K. P. J. R. P. A method for designing lifting configurations for high supersonic speeds, using axisymmetric flow fields. **Springer-Verlag**, 1968. Available at: https://www.scopus.com/pages/publications/12944274750.

KÜCHEMAN, D. **The Aerodynamic Design of Aircraft**. [*S.l.: s.n.*]: Pergamon Press, 1978. 564 p.

LI S., H. W. W. Z. Design and aerodynamic investigation of a parallel vehicle on a wide-speed range. **Science China Information Sciences**, 2014. Available at: https://doi.org/10.1007/s11432-014-5225-2.

LI S.; LUO, S. H. W. W. Z. Influence of the connection section on the aerodynamic performance of the tandem waverider in a wide-speed range. **Aerospace Science and Technology**, 2013. Available at: https://doi.org/10.1016/j.ast.2013.07.003.

LIU J.; DING, F. H. W. J. L. Novel approach for designing a hypersonic gliding–cruising dual waverider vehicle. **Acta Astronautia 102**, 2014. Available at: https://www.sciencedirect.com/science/article/pii/S0094576514001490.

MACROLAND A.D.; RANDOLPH, J. Hypersonic maneuvering to provide gravity assist. **AIAA**, 1990.

MANGIN B.; BENAY, R. C. B. C. A. Optimization of viscous waveriders derived from axisymmetric power-law blunt body flows. **American Institute of Aeronautics and Astronautics**, 2006. Available at: https://arc.aiaa.org/doi/10.2514/1.20079.

MOLDER, S. Internal, axisymmetric, conical flow. **American Institute of Aeronautics and Astronautics**, 1967. Available at: https://arc.aiaa.org/doi/10.2514/3.4179.

MORAN J. H.; MCQUELLIN, L. P. L. N. A. J. M. D. Z. F. Wind-tunnel based free-flight testing of a viscous optimised hypersonic waverider. **American Institute of Aeronautics and Astronautics**, 2023. Available at: https://doi.org/10.2514/6.2023-1385.vid.

NASA. Soarex (sub orbit al aerodynamic re entry experiments). **NASA**, 1998. Available at: Nasa.gov/centers/ames/research/technologyonepagers/soarex.html.

NONWEILER, T. Aerodynamic problems of manned space vehicles. **The Aeronautical Journal , Volume 63 , Issue 585**, 1959. Available at: https://doi.org/10.1017/S0368393100071662.

NONWEILER, T. Delta wings of shapes amenable to exact shock wave theory. **Journal of the Royal Aeronautical Society , Vol.67, Jan 1963, pp. 39**, 1962.

NORRIS G., W. G. Usaf's hypersonics road map sets long-term view). **Aviation Week Network**, 2012. Available at: https://aviationweek.com/defense/usafs-hypersonics-road-map-sets-long-term-view?check_logged_in=1.

OOSTROM, J. Effects of increasing aerothermodynamic fidelity on hypersonic trajectory optimisation for flight testing purposes. **Delft University of Technology**, 2015. Available at: https://repository.tudelft.nl/file/File_8019e00c-5996-4157-b79d-f0e6c8d81985?preview=1.

OSTAPENKO, N. Aerodynamic characteristics of v-shaped wings with shock waves detached from leading edges at hypersonic speeds. **Springer-Verlag**, 1993. Available at: https://doi.org/10.1007/BF01342691.

PALACIOS F.; PADRON, S. L. A. Stanford university unstructured (su2): Analysis and design technology for turbulent flows. **American Institute of Aeronautics and Astronautics**, 2014. Available at: https://doi.org/10.2514/6.2014-0243.

PENG B.; BINGYAN, C. C. J. C. L. Rapid design and optimization of waverider from 3d flow. **American Institute of Aeronautics and Astronautics**, 2016. Available at: https://arc.aiaa.org/doi/abs/10.2514/6.2016-3288.

PIKE, J. Efficient waveriders from known axisymmetric flow fields. **1st International Hypersonic Waverider Symposium**, 1990. Available at: https://ntrs.nasa.gov/citations/19910041105.

RASMUSSEN, M. Waverider configurations derived from inclined circular and elliptic cones. **J. SPACECRAFT**, 1980. Available at: https://doi.org/10.2514/3.57771.

RODI, P. Vortex lift waverider configurations. **American Institute of Aeronautics and Astronautics**, 2012. Available at: https://doi.org/10.2514/6.2012-1238.

RODI, P. Hypersonic waverider stream surface actuation for variable design point operation. **American Institute of Aeronautics and Astronautics**, 2016. Available at: https://doi.org/10.2514/6.2016-4706.

SILVA, B. Optimal preliminary design of hypersonic waverider using multiple metaheuristics. **Proceedings of the 72th International Astronautical Congress**, 2021.

SU2 Developers. **SU2 User Manual**. 2025. Available at: https://su2code.github.io/docs_v7/home/.

SZIROCZAK D.; SMITH, H. A review of design issues specific to hypersonic flight vehicles. **Progress in Aerospace Sciences**, 2016. Available at: https://doi.org/10.1016/j.paerosci.2016.04.001.

USAF. Usaf's hypersonics road map sets long-term view. **U.S. Air Force**, 2011. Available at: https://www.af.mil/About-Us/Fact-Sheets/Display/Article/104467/x-51a-waverider/.

WALKER S.H.; RODGERS, F. Falcon hypersonic technology overview. **AIAA 2005-3253**, 2012. Available at: https://doi.org/10.2514/6.2005-3253.

WANG, F. D. H. L. M. Aerodynamic characteristics research on wide-speed range waverider configuration. **Science China Technological Sciences**, 2009. Available at: https://doi.org/10.1007/s11431-009-0258-2.

ZHANG T.; WANG, Z. H. W. L. S. A design approach of wide-speed-range vehicles based on the cone-derived theory. **Aerospace Science and Technology**, 2017. Available at: https://doi.org/10.1016/j.ast.2017.09.010.

ZHAO Z.; HUANG, W. L. S. Z. T. Y. L. Variable mach number design approach for a parallel waverider with a wide-speed range based on the osculating cone theory. **Acta Astronautica**, 2018. Available at: https://doi.org/10.1016/j.actaastro.2018.04.008.

APPENDIX

APPENDIX A – GMSH .GEO CODE

```
SetFactory("OpenCASCADE");
//------------------------------------------------------------
//                    GEOMETRIA
//------------------------------------------------------------
// --- CUÑA (1000)---
// puntos
Point(1) = {0.0, 0.0, 0.0};          // arriba
Point(2) = {0.0, -0.185, 0.0};       // arriba
Point(3) = {1.0, -0.185, 0.0};       // arriba
Point(4) = {1.0, 0.0, 0.0};          // arriba
Point(5) = {1.0, 0.0, -0.170};       // abajo
Point(6) = {1.0, -0.185, -0.170};    // abajo
// líneas
Line(1) = {1, 2};  // arriba
Line(2) = {2, 3};  // arriba
Line(3) = {3, 4};  // arriba
Line(4) = {4, 1};  // arriba
Line(5) = {1, 5};  // lateral
Line(6) = {2, 6};  // lateral
Line(7) = {5, 4};  // vertical
Line(8) = {6, 3};  // vertical
Line(9) = {6, 5};  // fondo
// superficies
Line Loop(1) = {1, 2, 3, 4};   // arriba
Plane Surface(1001) = {1};
Line Loop(2) = {1, 6, 9, -5};  // abajo
Plane Surface(1002) = {2};
Line Loop(3) = {6, 8, -2}; // lateral
Plane Surface(1003) = {3};
Line Loop(4) = {5, 7, 4}; // lateral
Plane Surface(1004) = {4};
Line Loop(5) = {-3, -8, 9, 7}; // fondo
Plane Surface(1005) = {5};
// volumen
Surface Loop(1) = {1001, 1002, 1003, 1004, 1005};
Volume(1000) = {1};
```

```
// --- VOLUMEN DE CONTROL (2000) ---
// puntos
Point(7) = {-0.2, 0.0, 0.8};   // arriba
Point(8) = {-0.2, -0.8, 0.0};  // medio
Point(9) = {-0.2, 0.0, -0.8};  // abajo
Point(10) = {-0.2, 0.0, 0.0};  // centro
// líneas
Line(10) = {7, 9};
Circle(11) = {7, 10, 8};
Circle(12) = {8, 10, 9};
// superficies
Line Loop(7) = {12, -10, 11};   // arriba
Plane Surface(2001) = {7};
Extrude {2,0,0}{Surface{2001};}
BooleanDifference (2000) =  {Volume{1001}; Delete; } {Volume{1000}; Delete; };
// --- BOUNDARY CONDITIONS ---
Physical Surface("wall") = {6, 7, 8, 9};  // pared
Physical Surface("far") = {1, 2, 4, 5};  // far field
Physical Surface("symmetry") = {3};
Physical Volume("fluid") = {2000};
//------------------------------------------------------------
//                    MALLA
//------------------------------------------------------------
// --- PARÁMETROS GLOBALES ---
lc_far   = 0.030;   // lejos de la cuña
lc_wedge = 0.010;   // cerca de la pared de la cuña
lc_edge  = 0.005;   // bordes LE/TE
lc_wake  = 0.015;   // estela
//------------------ DISTANCIA A SUPERFICIES MOJADAS ------------------
alpha = 2.5*lc_wedge;  // ancho refinado
p     = 1.8;           // transición
Field[21] = Distance;
Field[21].SurfacesList = {7, 8, 9};
Field[22] = MathEval;
// lc(d) = lc_wedge + (lc_far - lc_wedge) * (1 - exp(-(d/alpha)^p))
Field[22].F = "0.01 + (0.03 - 0.01) * (1 - exp(- (F21/0.025)^1.8 ))";
//Field[22].F = "lc_wedge + (lc_far - lc_wedge)*(1 - exp(-(F21/alpha)^p))";
//------------------ LE y TE: REFINO ESPECÍFICO ------------------
Field[31] = Distance;
```

```
Field[31].CurvesList = {13, 15, 16};
Field[32] = Threshold;
Field[32].InField  = 31;
Field[32].SizeMin  = lc_edge;
Field[32].SizeMax  = lc_far;
Field[32].DistMin  = 1.5*lc_edge;
Field[32].DistMax  = 8.0*lc_edge;   // transición al far field
Field[32].StopAtDistMax = 1;
//-----------------  ESTELA: CAJA -------------------
xTE = 1.0;
Field[41] = Box;
Field[41].VIn  = lc_wake;
Field[41].VOut = lc_far;
Field[41].XMin = xTE;        Field[41].XMax = xTE +25.0*lc_wake;
Field[41].YMin = -0.185;     Field[41].YMax = 0.0;
Field[41].ZMin = -0.170;     Field[41].ZMax = 0.0;
//------------------  COMBINACIÓN -------------------
Field[99] = Min;
Field[99].FieldsList = {22, 32, 41};
Background Field = 99;
//------------------ OPCIONES EXTRAS ------------------
Mesh.CharacteristicLengthFromPoints = 0;
Mesh.CharacteristicLengthFromCurvature = 0;
Mesh.CharacteristicLengthExtendFromBoundary = 0;
Mesh.MinimumElementsPerTwoPi = 80;
Mesh.Algorithm3D = 4;
Mesh.Optimize = 1;
Mesh.OptimizeNetgen = 1;
```

APPENDIX B – SU2 CONFIGURATION FILE

```
% ----- DIRECT, ADJOINT, AND LINEARIZED PROBLEM DEFINITION ----%
%
% Physical governing equations (EULER, NAVIER_STOKES,
%                               WAVE_EQUATION, HEAT_EQUATION, FEM_ELASTICITY,
%                               POISSON_EQUATION)
SOLVER= EULER
%
% Mathematical problem (DIRECT, CONTINUOUS_ADJOINT)
MATH_PROBLEM= DIRECT
%
% Restart solution (NO, YES)
RESTART_SOL= NO
%
% --- COMPRESSIBLE AND INCOMPRESSIBLE FREE-STREAM DEFINITION --%
%
% Mach number (non-dimensional, based on the free-stream values)
MACH_NUMBER= 5.0
%
% Angle of attack (degrees)
AOA= 0.0
%
% Free-stream pressure (101325.0 N/m^2 by default, only Euler flows)
FREESTREAM_PRESSURE=  1151.4
%
% Free-stream temperature (288.15 K by default)
FREESTREAM_TEMPERATURE= 231.83

% -------------- REFERENCE VALUE DEFINITION -------------------%
%
% Reference origin for moment computation
REF_ORIGIN_MOMENT_X = 0.00
REF_ORIGIN_MOMENT_Y = 0.00
REF_ORIGIN_MOMENT_Z = 0.00
%
% Reference length for pitching, rolling, and yawing non-dimensional moment
REF_LENGTH= 1.0
```

```
%
% Reference area for force coefficients (0 implies automatic calculation)
REF_AREA= 0

% --------------- BOUNDARY CONDITION DEFINITION ---------------%
%
% Marker of the Euler boundary (NONE = no marker)
MARKER_EULER= (wall )
%
% Marker of the far field (NONE = no marker)
MARKER_FAR= (far)
MARKER_SYM= (symmetry)
AXISYMMETRIC = NO
%
% ---------------- SURFACES IDENTIFICATION --------------------%
%
% Marker(s) of the surface in the surface flow solution file
MARKER_PLOTTING = ( wall )
%
% Marker(s) of the surface where the non-dimensional coefficients are evaluated.
MARKER_MONITORING = ( wall )

% ----- COMMON PARAMETERS TO DEFINE THE NUMERICAL METHOD ------%
%
% Numerical method for spatial gradients (GREEN_GAUSS, WEIGHTED_LEAST_SQUARES)
NUM_METHOD_GRAD= WEIGHTED_LEAST_SQUARES
%
% Courant-Friedrichs-Lewy condition of the finest grid
CFL_NUMBER= 0.3
%
% Adaptive CFL number (NO, YES)
CFL_ADAPT= NO
%
% Parameters of the adaptive CFL number (factor down, factor up, CFL min value,
%                                        CFL max value )
CFL_ADAPT_PARAM= ( 1.1, 0.9, 5.0, 50.0 )
%
% Number of total iterations
ITER= 15000
```

```
% ---------------- LINEAR SOLVER DEFINITION -------------------%
%
% Linear solver for implicit formulations (BCGSTAB, FGMRES)
LINEAR_SOLVER= FGMRES
%
% Preconditioner of the Krylov linear solver (JACOBI, LINELET, LU_SGS)
LINEAR_SOLVER_PREC= LU_SGS
%
% Minimum error of the linear solver for implicit formulations
LINEAR_SOLVER_ERROR= 1E-6
%
% Max number of iterations of the linear solver for the implicit formulation
LINEAR_SOLVER_ITER= 5

% ------------------ MULTIGRID PARAMETERS ---------------------%
%
% Multi-Grid Levels (0 = no multi-grid)
MGLEVEL= 0
%
% Multi-grid cycle (V_CYCLE, W_CYCLE, FULLMG_CYCLE)
MGCYCLE= W_CYCLE
%
% Multi-Grid PreSmoothing Level
MG_PRE_SMOOTH= ( 1, 1, 1, 1 )
%
% Multi-Grid PostSmoothing Level
MG_POST_SMOOTH= ( 1, 1, 1, 1 )
%
% Jacobi implicit smoothing of the correction
MG_CORRECTION_SMOOTH= ( 0, 0, 0, 0 )
%
% Damping factor for the residual restriction
MG_DAMP_RESTRICTION= 0.75
%
% Damping factor for the correction prolongation
MG_DAMP_PROLONGATION= 0.75

% ------------ FLOW NUMERICAL METHOD DEFINITION ---------------%
```

```
%
% Convective numerical method (JST, LAX-FRIEDRICH, CUSP, ROE, AUSM, SLAU, SLAU2,
%                                AUSMPLUSUP, AUSMPLUSUP2 HLLC, TURKEL_PREC, MSW)
CONV_NUM_METHOD_FLOW= AUSM
%
% Monotonic Upwind Scheme for Conservation Laws (TVD) in the flow equations.
%           Required for 2nd order upwind schemes (NO, YES)
MUSCL_FLOW= NO
%
% Slope limiter (VENKATAKRISHNAN, MINMOD)
SLOPE_LIMITER_FLOW= BARTH_JESPERSEN
%
% Time discretization (RUNGE-KUTTA_EXPLICIT, EULER_IMPLICIT, EULER_EXPLICIT)
TIME_DISCRE_FLOW= EULER_IMPLICIT

% ------------------- CONVERGENCE PARAMETERS ------------------%
%
% Min value of the residual (log10 of the residual)
CONV_RESIDUAL_MINVAL= -15
%
% Start Cauchy criteria at iteration number
CONV_STARTITER= 10
%
% Number of elements to apply the criteria
CONV_CAUCHY_ELEMS= 100
%
% Epsilon to control the series convergence
CONV_CAUCHY_EPS= 1E-6
%

% ----------------- INPUT/OUTPUT INFORMATION ------------------%
% Mesh input file
MESH_FILENAME= wedge_definitivo_metros.su2
%
% Mesh input file format (SU2, CGNS, NETCDF_ASCII)
MESH_FORMAT= SU2
%
% Mesh output file
MESH_OUT_FILENAME= mesh_out_05.su2
```

```
%
% Restart flow input file
SOLUTION_FILENAME= restart_flow_05.dat
%
% Restart adjoint input file
SOLUTION_ADJ_FILENAME= solution_adj_05.dat
%
TABULAR_FORMAT= CSV
%
% Output file convergence history (w/o extension)
CONV_FILENAME= history_05
%
% Output file restart flow
RESTART_FILENAME= restart_flow_05.dat
%
% Output file restart adjoint
RESTART_ADJ_FILENAME= restart_adj_05.dat
%
% Output file flow (w/o extension) variables
VOLUME_FILENAME= flow_05
%
% Output file adjoint (w/o extension) variables
VOLUME_ADJ_FILENAME= adjoint_05
%
% Output Objective function gradient (using continuous adjoint)
GRAD_OBJFUNC_FILENAME= of_grad_05.dat
%
% Output file surface flow coefficient (w/o extension)
SURFACE_FILENAME= surface_flow_05
%
% Output file surface adjoint coefficient (w/o extension)
SURFACE_ADJ_FILENAME= surface_adjoint_05
%
% Writing solution file frequency
OUTPUT_WRT_FREQ= 500
%
% Screen output
SCREEN_OUTPUT= (INNER_ITER, RMS_DENSITY, RMS_ENERGY, LIFT, DRAG)
```